Metal Compound-Based Electrocatalysts for Hydrogen Peroxide Electrosynthesis and the Electro-Fenton Process

Hongyuan Sheng, R. Dominic Ross, J. R. Schmidt, and Song Jin**

Department of Chemistry, University of Wisconsin—Madison, 1101 University Avenue, Madison, Wisconsin 53706, United States

*Corresponding author emails: schmidt@chem.wisc.edu; jin@chem.wisc.edu

ABSTRACT

Hydrogen peroxide (H_2O_2) is a powerful oxidant with many applications, but its chemical production is unsustainable and unsafe. Decentralized electrosynthesis of H_2O_2 via the selective two-electron oxygen reduction reaction ($2e^-$ ORR) is attractive, which demands active, selective, stable, and cost-effective electrocatalysts in acidic and neutral solutions where H_2O_2 is stable. Metal compounds are an emerging class of $2e^-$ ORR catalysts with diverse and tunable structural motifs for optimizing H_2O_2 electrosynthesis, yet remain underexplored with poorly understood structure-property relationships. This Focus Review summarizes the recent computational and experimental developments of metal compound-based acidic and neutral $2e^-$ ORR catalysts, and the resultant mechanistic understanding and catalyst design rules for guiding future catalyst discoveries. The many fundamental and practical factors at the reaction, catalyst, electrode, and device level that impact H_2O_2 electrosynthesis are systematically discussed. Metal compound-based acidic $2e^-$ ORR catalysts can also enable efficient electro-Fenton process for environmental remediation and biomass valorization.

TOC Graph

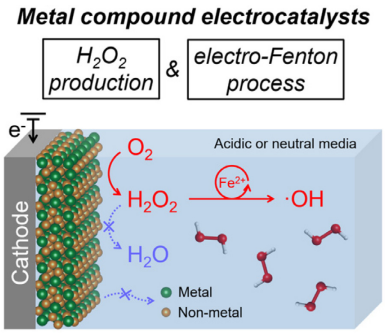

Hydrogen peroxide (H_2O_2) is a powerful and green oxidant with diverse applications in chemical manufacturing, wastewater treatment, and the paper and pulp industry.[1] The COVID-19 pandemic has also contributed to the recent rapid growth of the global H_2O_2 market for use in disinfection.[2] The industrial production of H_2O_2 proceeds chemically through the anthraquinone process and is energy- and waste-intensive. It consumes H_2 gas, involves extraction of H_2O_2 from organic solvents into the aqueous phase, produces up to 70 wt% concentrated H_2O_2 by distillation, and requires hazardous transportation from centralized plants to the point-of-use.[1] Decentralized electrosynthesis of H_2O_2 via the two-electron oxygen reduction reaction ($2e^-$ ORR, $O_2 + 2\ H^+ + 2\ e^- \rightarrow H_2O_2$),[3-6] which is typically coupled with oxygen evolution reaction ($2\ H_2O \rightarrow O_2 + 4\ H^+ + 4\ e^-$) in aqueous solutions but could also be paired with the anodic electrosynthesis of other value-added chemicals,[7, 8] may offer a more sustainable route. It can be driven by the increasingly affordable renewable electricity,[9] eliminate the need for H_2 gas, operate under ambient conditions, and produce dilute H_2O_2 directly at the point-of-use, which is advantageous for distributed applications such as water treatment that requires <0.1 wt% H_2O_2.[3] The key challenge is to develop robust and inexpensive electrocatalysts with high activity, selectivity, and stability for the desired $2e^-$ reduction to H_2O_2 (vs. the competing $4e^-$ reduction to

water). H_2O_2 can also be electrogenerated by the two-electron water oxidation reaction ($2\ H_2O \rightarrow H_2O_2 + 2\ H^+ + 2\ e^-$),[10] but this Focus Review focuses only on the $2e^-$ ORR approach.

Over the last decade, several classes of selective $2e^-$ ORR catalysts, including noble metal alloys,[11-13] carbon nanomaterials,[14-16] single-atom catalysts,[17-21] and metal compounds,[22-27] have been studied for H_2O_2 electrosynthesis under different pH conditions.[3, 6] Among these reports, alkaline $2e^-$ ORR catalysts have been most extensively studied, despite several limitations in alkaline H_2O_2 electrosynthesis including the instability of H_2O_2 in alkaline solution[28] and the less competitive anion exchange membrane (AEM) technology.[3] Moreover, carbon nanomaterials already perform quite well under alkaline conditions.[3, 6] In contrast, the less studied acidic and neutral conditions are attractive for several reasons besides the chemical stability of H_2O_2. Acidic H_2O_2 electrosynthesis can proceed in the technologically mature proton exchange membrane (PEM) devices.[3] On-site water disinfection and environmental remediation can also benefit from acidic H_2O_2 electrosynthesis because the electro-Fenton process operates at the optimum pH of ~3 to convert the produced H_2O_2 into the more oxidizing hydroxyl radical (·OH) for the removal of persistent bacteria and organic pollutants.[29] For direct applications, the noncorrosive neutral solutions can avoid the need for neutralization.[16, 18, 21, 26] However, high-performance yet cost-effective $2e^-$ ORR catalysts in acidic and neutral solutions are still being developed.

In comparison to the well-studied carbon nanomaterials and noble metal alloys, interest in metal compounds as potential $2e^-$ ORR catalysts for H_2O_2 electrosynthesis is more recent and their structure-property relationships are much less understood. By integrating computation and experiment, our recent research established rational catalyst design rules that led to the discovery of a series of binary (CoS_2,[22] $CoSe_2$,[23] $NiSe_2$[24]) and quaternary ($CuCo_{2-x}Ni_xS_4$, $0 \leq x \leq 1.2$[25]) earth-abundant metal chalcogenide compounds as robust $2e^-$ ORR catalysts in acidic and neutral

solutions, and achieved mechanistic insights into the catalyst selectivity, activity, and stability. In the meantime, other metal compounds have also found success in selective $2e^-$ ORR electrocatalysis and H_2O_2 electrosynthesis.[26, 27, 30-33] The systematic studies of metal chalcogenide catalysts for acidic $2e^-$ ORR has led to significant improvements in both H_2O_2 bulk electrosynthesis performance and catalyst stability, and the more stable $CoSe_2$[23] and $NiSe_2$[24] catalysts have been utilized for the electro-Fenton process[29] that is more demanding for catalyst stability. In addition to demonstrating electro-Fenton degradation of an organic pollutant using a $CoSe_2$ cathode,[23] we further developed a novel approach for electrochemical valorization of biomass-derived feedstock into value-added oxidation products using the electro-Fenton process at a $NiSe_2$ cathode.[24]

This Focus Review aims to provide a concise summary and outlook of metal compound-based $2e^-$ ORR catalysts for acidic and neutral H_2O_2 electrosynthesis and the subsequent electro-Fenton process enabled by these new catalysts (Figure 1). We start with the computational frameworks for predictive identification of stable metal compounds that are selective and active toward $2e^-$ ORR. We then overview the experimental practices for rigorously evaluating metal compound-based $2e^-$ ORR catalysts, from basic electrochemical techniques to catalyst leaching and side reaction monitoring, and to scaled-up H_2O_2 bulk electrosynthesis and electrochemical device engineering. The uses of metal compound-based cathodes in the electro-Fenton process are then discussed for various potential applications from environmental treatment to valuable chemical transformations. Finally, future challenges and opportunities in search of new better-performing metal compound-based $2e^-$ ORR catalysts are proposed.

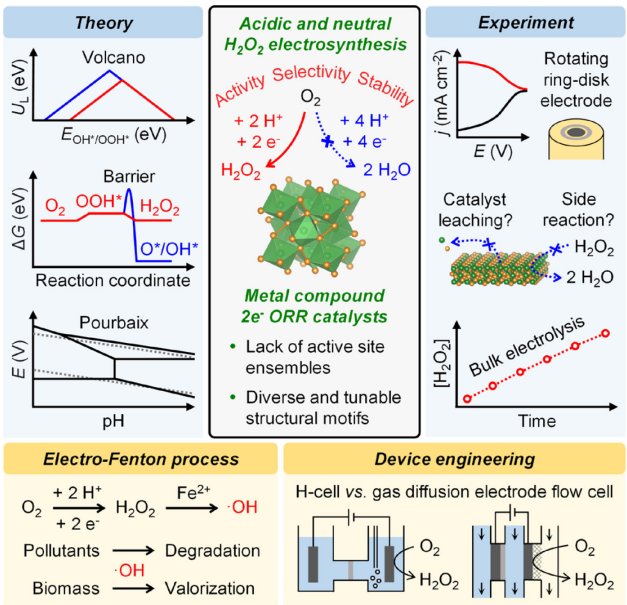

Figure 1. Schematic outline for studying and developing metal compound-based electrocatalysts for acidic and neutral H_2O_2 electrosynthesis and the electro-Fenton process.

Fundamentals of Selective 2e⁻ ORR on Metal Compound-Based Catalysts

Thermodynamic Considerations. The thermodynamics of 2e⁻ ORR ($O_2 + 2\ H^+ + 2\ e^- \rightarrow H_2O_2$, E^o = 0.69 V vs. reversible hydrogen electrode, RHE) and 4e⁻ ORR ($O_2 + 4\ H^+ + 4\ e^- \rightarrow 2\ H_2O$, E^o = 1.23 V vs. RHE) are often described by the volcano relations between the thermodynamic limiting potential (U_L) and the energetics of key reaction intermediates.[34] 2e⁻ ORR proceeds via the adsorption of OOH* ($O_2 + * + H^+ + e^- \rightarrow$ OOH*, where * is an unoccupied surface binding site) followed by its desorption to form H_2O_2 (OOH* + H^+ + $e^- \rightarrow H_2O_2$ + *); 4e⁻ ORR occurs via the O-O bond cleavage processes (thermal cleavage: O_2 + 2 * → 2 O*, and OOH* + * → O* + OH*; electrochemical reductive elimination: OOH* + H^+ + e^- → O* + H_2O).[22] The key intermediates of 2e⁻ ORR (OOH*) and 4e⁻ ORR (OH*) follow a linear scaling relationship (typically $\Delta G_{OOH*} = \Delta G_{OH*} + 3.2$ eV[34]), resulting in the 2e⁻ and 4e⁻ ORR

volcanos (Figure 2a).[6] The 2e⁻ ORR activity, determined by the OOH* adsorption energy (ΔG_{OOH*}), is maximized at the peak of 2e⁻ ORR volcano. Moving leftwards from 2e⁻ ORR volcano peak, the catalyst surface binds OOH* (and OH*) more strongly, and U_L of 4e⁻ ORR is always more positive than that of 2e⁻ ORR, indicating the 4e⁻ pathway will dominate because there is a greater driving force to form H_2O than H_2O_2 (Figure 2a, blue region). To the right of 2e⁻ ORR volcano peak (Figure 2a, green region), U_L of the 2e⁻ and 4e⁻ pathways overlap, which means that the selectivity for 2e⁻ vs. 4e⁻ ORR will be a complex interplay determined by kinetics (see the section below), and moving rightwards will lower the activity for both 2e⁻ and 4e⁻ ORR because the formation of OOH* and OH* become more difficult. Note that the as-mentioned linear scaling relationship is derived for catalyst surfaces where all reaction intermediates bind to identical adsorption sites. Catalysts with differing structural motifs, like metal compounds, may break such relationship by changing the adsorption sites for different reaction intermediates, e.g., destabilizing O* relative to OOH*, which may offer new opportunities for improving the 2e⁻ ORR selectivity.[11, 35]

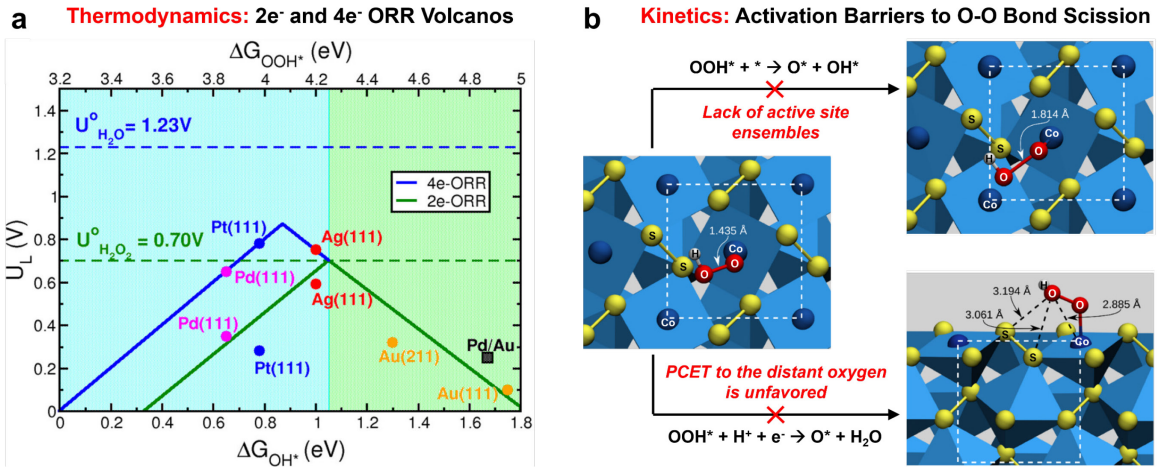

Figure 2. Thermodynamic and kinetic considerations of ORR pathways. (a) $2e^-$ ORR (green trace) and $4e^-$ ORR (blue trace) volcano plots using examples of noble metals. Shaded green (weak OOH* binding) and blue (strong OOH* binding) areas represent the regions with high selectivity for $2e^-$ and $4e^-$ pathway, respectively. Reprinted from ref. [6]. Copyright 2020 American Chemical Society. (b) $2e^-$ ORR selectivity can be kinetically controlled by increasing the activation barriers to the O-O bond cleavage processes, as illustrated on the CoS_2 (100) surface that lacks active site ensembles. Source pictures in (b) are adapted from ref. [22]. Copyright 2019 American Chemical Society.

Kinetic Considerations. The recent studies of $2e^-$ ORR catalysts often only consider the thermodynamics of the ORR pathways based on the volcano relations (Figure 2). However, the kinetic considerations of suppressing the undesired O-O bond cleavage are also important (Figure 2b), as they laid the foundation for our recent discovery of a series of metal compound-based new $2e^-$ ORR catalysts.[22-24] OOH* can be cleaved thermally across two adjacent active sites or electrochemically via reductive elimination, which can be thermodynamically suppressed by destabilizing O* and/or OH* on the catalyst surface (vide supra). These O-O bond cleavage processes can also be kinetically suppressed by increasing their activation barriers, and one effective strategy is to increase the interatomic distances between neighboring active sites on the catalyst surface. Take the recently established CoS_2 catalyst[22] as an example, where the Co active sites are spatially separated by disulfide anions in the crystal lattice, and the Co-Co interatomic distance (3.941 Å) is much longer than the O-O bond length in OOH* (Figure 2b, left). To thermally cleave OOH* onto neighboring Co active sites, the transition state requires not only substantial elongation of the O-O bond by ~0.4 Å but also significant lattice distortion of CoS_2 to

shorten the Co-Co distance, resulting in a high activation barrier of 0.61 eV (Figure 2b, top path). This observation lies in sharp contrast to close-packed pure metal surfaces which display minimal activation barriers for rapid OOH* scission (0.06, 0.16, and 0.06 eV on (111) facet of Pd, Pt, and Cu).[36] Moreover, due to the lack of active site ensembles in CoS_2, only one of the oxygen atoms in OOH* interacts closely with the CoS_2 surface. Unlike the more facile proton-coupled electron transfer (PCET) to the surface-bound oxygen (forming H_2O_2), reductive elimination of OOH* is unfavored because PCET to the distant oxygen requires through-space transfer (~3 Å) or tunneling through the O-O bond (Figure 2b, bottom path). This kinetic suppression of O-O bond cleavage could serve as one of the general design principles in search of more selective $2e^-$ ORR catalysts based on metal compounds.

Merits of Metal Compounds as $2e^-$ ORR Catalysts. Metal compounds remain underexplored as $2e^-$ ORR catalysts for H_2O_2 electrosynthesis, but the mechanistic discussions suggest that metal compounds offer many exciting attributes for tailoring catalytic properties for $2e^-$ ORR. Unlike pure metals where all surface adsorbates bind to identical adsorption sites and follow linear scaling relationship, the presence of several distinct (metal and nonmetal) binding sites on metal compound surfaces allow for independently tunable binding energies of surface adsorbates (OOH* vs. OH* vs. O*), which could potentially break such conventional scaling relationship for optimizing $2e^-$ ORR electrocatalysis. The dispersed metal sites, separated by nonmetal atoms in crystal lattices, suppress the undesired O-O bond cleavage. Well-defined crystalline and multi-elemental motifs provide diverse yet controllable structural and electronic tunability (composition and phase control,[22-25] doping and vacancy engineering[37, 38]) for achieving optimized selectivity, activity, and stability toward $2e^-$ ORR. Therefore, opportunities

for developing high-performance $2e^-$ ORR catalysts based on metal compounds remain underexplored. This Focus Review illustrates these benefits and untapped opportunities.

Computational Design of Metal Compound-Based $2e^-$ ORR Catalysts

Stability Screening Using Bulk Pourbaix Diagrams and Surface Adsorbate Analyses. The electrochemical stability is one of the most important factors for metal compound-based electrocatalysts, which can be predicted by density functional theory (DFT) calculations. The bulk phase stability of a metal compound in aqueous environment is described by its bulk Pourbaix diagram, which maps the Gibbs free energy difference with respect to its Pourbaix stable domain (ΔG_{pbx}) as a function of potential and pH. It is freely available from the Materials Project database[39] and available for retrieval and analysis via its Python-based application programming interface (API).[40] Depending on the energy barriers for bulk decomposition reactions and the nature of decomposition products, the bulk of metal compounds can remain stable when ΔG_{pbx} is up to 0.5 eV/atom.[41] Beyond bulk stability, the surface stability of a metal compound against corrosion and reconstruction can be examined as a function of potential at a given pH, via the Gibbs free energy change associated with the adsorption of O* and/or OH* on the surface when in equilibrium with water. This is usually referred to as surface Pourbaix diagram when the most stable surface termination is plotted as a function of both potential and pH.[42, 43] Although bulk Pourbaix diagrams and surface oxygen adsorbate energetics/surface Pourbaix diagrams are often employed for elucidating the (in)stability of metal compound-based catalysts for hydrogen evolution reaction (HER)[44] or oxygen evolution reaction (OER)[45] in corrosive acidic solutions, such stability assessments are infrequently performed in the recent studies of $2e^-$ ORR catalysts.

Our recent studies on binary metal dichalcogenide-based acidic $2e^-$ ORR catalysts[22-24] have routinely examined bulk Pourbaix diagrams and surface oxygen adsorbate energetics, allowing us to develop mechanistic understanding and rational design rules for stable metal compound-based $2e^-$ ORR catalysts and achieve significantly improved catalyst stability. We computationally screened the stability of a series of metal compounds: cubic pyrite-type *c*-CoS_2, *c*-$CoSe_2$, *c*-$NiSe_2$, and orthorhombic marcasite-type *o*-$CoSe_2$ (Figure 3a). The O* and OH* binding strengths on the most stable facets of these compounds display general trends depending on the nature of chalcogen and metal (Figure 3b). For CoS_2 and both $CoSe_2$ polymorphs, the chalcogen is the preferential binding site for O*, but O* binds substantially more strongly to S than to Se by 0.59 eV at the calculated standard equilibrium potential of $2e^-$ ORR (U^o_{RHE}). Such difference suggests that CoS_2 is more prone to surface oxidation, which occurs at the S site to form highly soluble SO_4^{2-}, followed by Co^{2+} leaching and catalyst degradation. This is also consistent with a recent report that combines bulk and surface Pourbaix diagrams to show the dissolution of CoS_2 surface and a high surface coverage of O* at S sites are expected at pH < 8 and potentials > 0.5 V vs. RHE.[46] Switching from $CoSe_2$ to $NiSe_2$ results in a change in the O* preferential binding site from Se to Ni, suggesting that $NiSe_2$ is even more resistant to surface oxidation than both $CoSe_2$ polymorphs because of the low affinity of O* to its Se site. In addition, the OH* binding strength to Ni is much weaker that to Co, which helps stabilizing the adsorbate-free clean surface of $NiSe_2$, relative to the surfaces adsorbed with OH* (and/or O*), over a wide potential range (yellow region in Figure 3c). Overall, the DFT-predicted surface stability follows the order of *c*-$NiSe_2$ > (*c*-$CoSe_2$ ≈ *o*-$CoSe_2$) > *c*-CoS_2, in agreement with the bulk phase stability indicated by the Materials Project database.[22-24] Note that O* and OH* can also form during ORR if the O-O bond cleavage takes place (Figure 2b). Therefore, these surface oxygen

adsorbate analyses can be readily generalized for stability screening of various metal compounds under aqueous environments and ORR operating conditions.

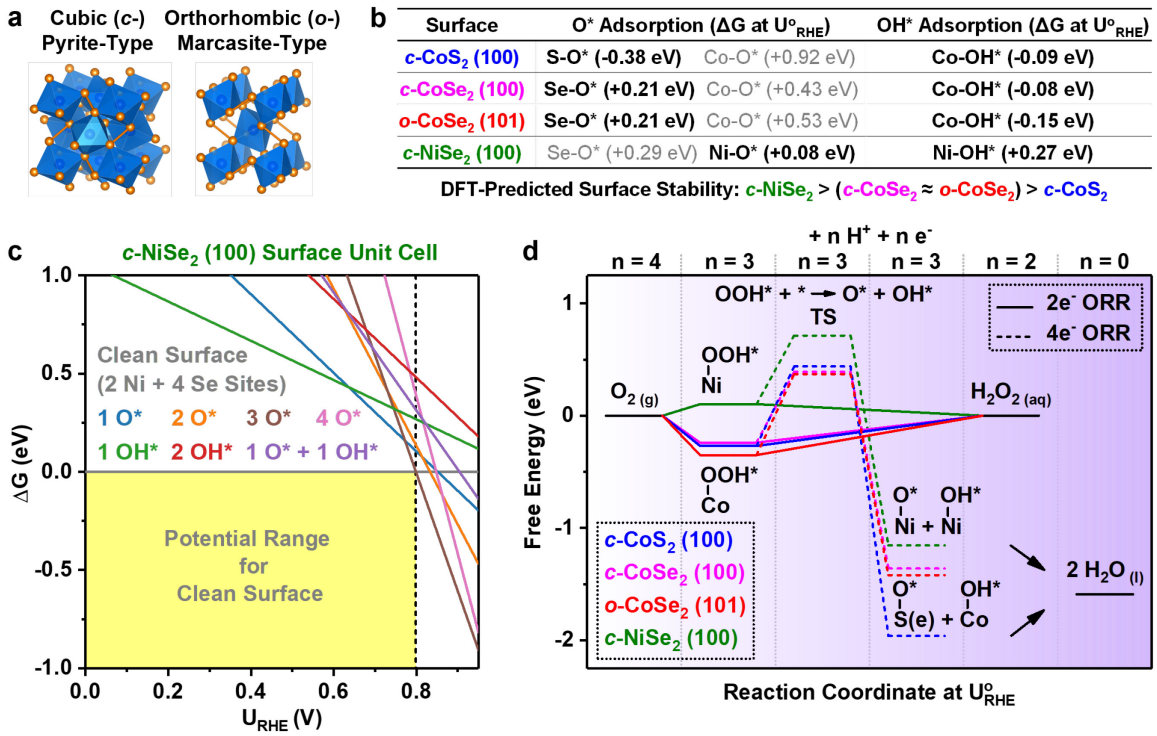

Figure 3. Computational screening of stability, selectivity, and activity of binary metal compound-based $2e^-$ ORR catalysts (*c*-CoS_2, *c*-$CoSe_2$, *o*-$CoSe_2$, and *c*-$NiSe_2$). (a) Crystal structures of pyrite- and marcasite-type metal chalcogenides. (b) Energetics of O* and OH* adsorption to their preferential binding sites on the most stable facets of *c*-CoS_2, *c*-$CoSe_2$, *o*-$CoSe_2$, and *c*-$NiSe_2$. Note that the entry for the Ni-O^* displays a O^* atom bridging the Ni and Se atoms. (c) Comparisons of free energies of different O* and/or OH* coverages on *c*-$NiSe_2$ (100) surface unit cell comprising two Ni and four Se sites. For 3 O* and 4 O* coverages, two O* bind to Ni, and the rest of O* bind to Se. For the other O* and/or OH* coverages, all adsorbates bind to Ni. (d) Free energy diagrams of the $2e^-$ and $4e^-$ ORR pathways. The transition state for OOH* cleavage (OOH* + * → O* + OH*) is denoted as TS. The reaction coordinate is denoted as +

n H^+ + n e^-, where n ranges from 0 to 4. Source pictures in panel (a) are adapted from ref. [23]. Copyright 2020 Royal Society of Chemistry. Source data for *c*-CoS_2, *c*-$CoSe_2$, and *o*-$CoSe_2$ in panels (b) and (d) are adapted from ref. [23]. Copyright 2020 Royal Society of Chemistry. Source data for *c*-$NiSe_2$ in panels (b)–(d) are adapted from ref. [24]. Copyright 2022 Springer Nature Limited.

Selectivity and Activity Assessments by Free Energy Diagrams. The selectivity and activity for $2e^-$ ORR can be computationally assessed via free energy diagrams of the desired $2e^-$ and competing $4e^-$ ORR pathways (Figure 3d).[22-24] Recent reports showed that all four binary metal dichalcogenides (*c*-CoS_2, *c*-$CoSe_2$, *o*-$CoSe_2$, and *c*-$NiSe_2$) are expected to be selective and active for $2e^-$ ORR because they exhibit similarly high activation barriers to the undesired OOH* cleavage (0.61 to 0.72 eV at U^o_{RHE}, top dashed traces in Figure 3d), and nearly thermoneutral OOH* adsorption at U^o_{RHE} (solid traces in Figure 3d). The differences among these metal dichalcogenides lie in the adsorption energetics of the reaction intermediate(s) of $2e^-$ ORR (OOH*) and $4e^-$ ORR (O* and OH*). Changing the metal from Co to Ni weakens the OOH* adsorption, making *c*-$NiSe_2$ situated on the weak OOH* binding leg of the $2e^-$ ORR volcano. In contrast, *c*-CoS_2, *c*-$CoSe_2$, and *o*-$CoSe_2$ are all situated on the strong OOH* binding leg. As the $2e^-$ ORR selectivity can be influenced by the OOH* adsorption energy (Figure 2a), *c*-$NiSe_2$ could be even more selective for $2e^-$ ORR than Co-based chalcogenides. Changing the chalcogen from S to Se and the metal from Co to Ni collectively weaken the O* and OH* adsorption and destabilize the $4e^-$ ORR intermediates (bottom dashed traces in Figure 3d), which also promotes the $2e^-$ ORR pathway. By combining thermodynamic analysis of ORR pathways and the kinetic barriers associated with O-O bond cleavage processes, these computational frameworks serve as

predictive tools for unveiling general trends in the $2e^-$ ORR selectivity and activity of metal compound-based catalysts. To conclude the prior computational discussions, the general design principles for metal compound-based $2e^-$ ORR catalysts include optimizing OOH* adsorption for activity, kinetically suppressing O-O bond cleavage for selectivity, and destabilizing surface oxygen adsorbates for stability.

Experimental Studies of Metal Compound-Based $2e^-$ ORR Catalysts

Rotating Ring-Disk Electrode Evaluation. Use of a rotating ring-disk electrode (RRDE) comprising a glassy carbon disk and a Pt ring offers facile assessments of the $2e^-$ ORR catalytic properties of solid catalysts, including the selectivity. Usually powders of the catalysts are mixed up with additives as catalyst inks and drop-cast onto the disk to make a uniform catalyst film for the RRDE measurements. We caution the use of carbon additives in catalyst film since carbon materials exhibit nontrivial $2e^-$ ORR activities especially under alkaline and neutral pH.[14] Similar attention should be paid to the glassy carbon disk as it also catalyzes $2e^-$ ORR under alkaline pH.[3] The $2e^-$ ORR activity and selectivity can be evaluated in an undivided three-electrode cell with a reference electrode and a graphite counter electrode at a certain rotation rate in O_2-saturated electrolyte solution, where linear sweep voltammetry (LSV) is applied to the disk for catalyzing ORR, meanwhile the ring is held at a constant potential (1.2 to 1.3 V vs. RHE) for selective and diffusion-limited oxidation of the produced H_2O_2. When evaluating $2e^-$ ORR at neutral pH, it is crucial to use buffered electrolyte solution to avoid the alkaline shift of the local pH near the electrode since ORR consumes protons. The potential range for LSV on the disk should not exceed the electrochemical stability window of the catalyst,

which is indicated by bulk Pourbaix diagrams and surface oxygen adsorbate energetics (vide supra). LSV scans for representative metal chalcogenide catalysts are shown in Figure 4a.

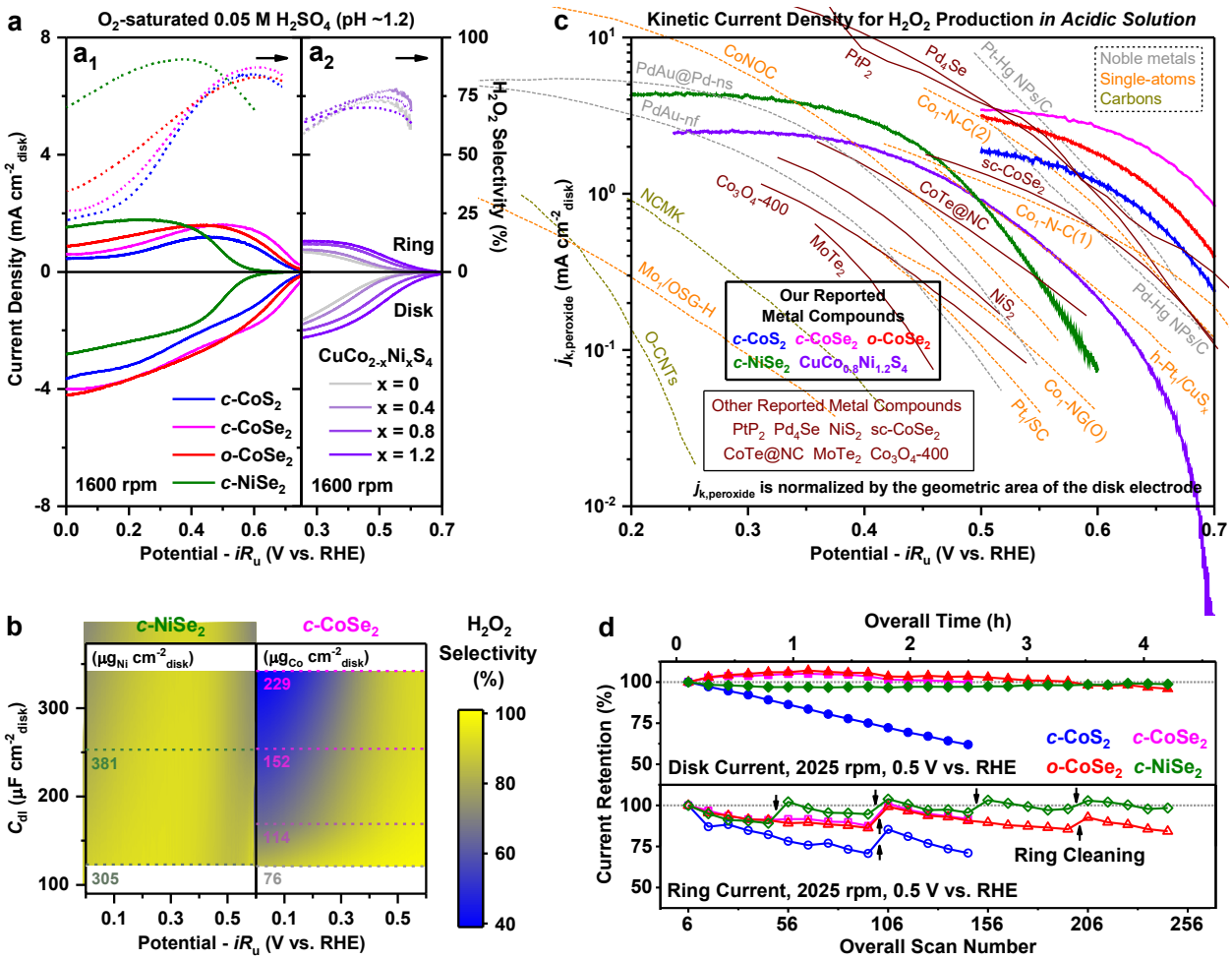

Figure 4. RRDE assessments of representative metal chalcogenide 2e$^-$ ORR catalysts. (a) RRDE voltammograms and the corresponding H_2O_2 selectivity of (a_1) binary metal chalcogenide (*c*-CoS_2,[22] *c*-$CoSe_2$,[23] *o*-$CoSe_2$,[23] *c*-$NiSe_2$[24]) and (a_2) quaternary thiospinel ($CuCo_{2-x}Ni_xS_4$, $0 \leq x \leq 1.2$[25]) catalysts at 1600 rpm in O_2-saturated 0.05 M H_2SO_4. (b) The H_2O_2 selectivity plotted against potential and double-layer capacitance (C_{dl}) for *c*-$NiSe_2$ vs. *c*-$CoSe_2$ from RRDE experiments at 1600 rpm in 0.05 M H_2SO_4. (c) Comparisons of kinetic current densities for H_2O_2 production ($j_{k,peroxide}$) on metal compound-based 2e$^-$ ORR catalysts vs. other classes of 2e$^-$ ORR

catalysts recently reported based on RRDE experiments at 1600 rpm in acidic solution. (d) RRDE stability test of *c*-CoS_2 vs. *c*-$CoSe_2$ vs. *o*-$CoSe_2$ vs. *c*-$NiSe_2$ in 0.05 M H_2SO_4. Source data for *c*-CoS_2, *c*-$CoSe_2$, and *o*-$CoSe_2$ in panels (a), (c), and (d) are adapted from ref. [23]. Copyright 2020 Royal Society of Chemistry. Source data for *c*-$CoSe_2$ in panel (b), and source data for *c*-$NiSe_2$ in panels (a)–(d) are adapted from ref. [24]. Copyright 2022 Springer Nature Limited. Source data for $CuCo_{2-x}Ni_xS_4$ in panels (a) and (c) are adapted from ref. [25]. Copyright 2021 American Chemical Society. Detailed catalyst and electrode information are described in Table S1 in the Supporting Information.

After subtracting background current (recorded under Ar-saturated condition) from disk current (i_{disk}) and ring current (i_{ring}), the H_2O_2 selectivity (p_{RRDE}) is calculated as: $p_{RRDE} = \frac{\frac{i_{ring}}{N}}{i_{disk}+\frac{i_{ring}}{N}} \times 100\%$, where N is the collection efficiency (calibrated using a ferri-/ferrocyanide redox couple). This RRDE method of determining H_2O_2 selectivity is more accurate than the Koutecky-Levich method that is often employed.[47] We note that the measured H_2O_2 selectivity by RRDE can depend on the areal catalyst loading,[22-25] therefore measuring the double-layer capacitance (C_{dl}) and the associated electrochemically active surface area (ECSA) of catalyst films by performing cyclic voltammetry (CV) in non-Faradaic potential region under Ar-saturated condition is critical for fair comparisons of the $2e^-$ ORR selectivity and activity. Figure 4a summarizes the representative RRDE assessments of our recently established binary metal dichalcogenide[22-24] and quaternary thiospinel[25] $2e^-$ ORR catalysts in 0.05 M H_2SO_4 solution.

RRDE case studies I: Each binary metal chalcogenide catalyst (*c*-CoS_2,[22] *c*-$CoSe_2$,[23] *o*-$CoSe_2$,[23] *c*-$NiSe_2$[24]) was tested at various catalyst loadings, and their optimum overall electrode

performances for H_2O_2 production (i.e., high partial current density at small overpotential) were achieved at high catalyst loadings (shown in Figure 4a$_1$). All three Co-based chalcogenides exhibit similarly high 2e$^-$ ORR activity as they require nearly zero overpotential for the catalytic onset. They show high H_2O_2 selectivity (up to 86%) in the low overpotential region, but the H_2O_2 selectivity decreases with increasing overpotential at high catalyst loadings. This potential-dependent H_2O_2 selectivity indicates the undesired O-O bond cleavage processes dominate at large overpotentials on these Co-based catalysts.[22, 23] In comparison, the 2e$^-$ ORR catalytic onset potential on $NiSe_2$ is less positive, but its H_2O_2 selectivity shows relatively little dependence on overpotential and remains high (up to 90%) over a wide potential range.[24] Such differences in the H_2O_2 selectivity profiles of $NiSe_2$ vs. Co-based chalcogenides could result from several possible causes: (1) the weaker OOH* binding to Ni than to Co (by 0.34 to 0.45 eV[22-24]) makes $NiSe_2$ and Co-based chalcogenides situated on the different legs of 2e$^-$ ORR volcano (see Figure 3a), which could affect the 2e$^-$ ORR selectivity (vide supra); (2) the weaker OH* binding to Ni than to Co (by 0.35 to 0.42 eV, see Figure 3b) relatively destabilizes this 4e$^-$ ORR intermediate on $NiSe_2$, which could promote 2e$^-$ ORR. Co-based chalcogenides tested at low catalyst loadings show less dramatic decrease in H_2O_2 selectivity with increasing overpotential, and their H_2O_2 selectivity profiles become more similar to that of $NiSe_2$ (Figure 4b). Future theoretical and experimental studies are needed to examine the various competing catalytic processes in greater details and elucidate the complex dependence of H_2O_2 selectivity on overpotential and catalyst loading, which will accelerate the discovery of more selective metal compound-based 2e$^-$ ORR catalysts.

RRDE case studies II: The series of quaternary thiospinel ($CuCo_{2-x}Ni_xS_4$, $0 \leq x \leq 1.2$) catalysts serve as an example of the systematic modification of the 2e$^-$ ORR catalytic properties of metal compounds by compositional tuning.[25] The crystal structure of $CuCo_{2-x}Ni_xS_4$ thiospinels

(Figure 5a) exhibits mixed coordination environments around metal centers that occupy tetrahedral and/or octahedral sites, which can be experimentally characterized by their extended X-ray absorption fine structures (EXAFS) at the constituent metal K-edges (Figure 5b) using X-ray absorption spectroscopy (XAS). The series of catalysts were electrochemically tested at a constant catalyst loading with similar C_{dl} values across all samples (Table S1), guaranteeing that the observed differences in their catalytic properties were intrinsic and not a result of changing the catalyst surface areas. Their RRDE voltammograms (Figure 4a$_2$) show that incorporating greater amount of Ni in the thiospinel catalyst systematically increases $2e^-$ ORR activity without compromising high H_2O_2 selectivity (up to 78%), and the crystal structure of thiospinel is preserved when the Ni content increases (up to x = 1.2), as confirmed by powder X-ray diffraction (Figure 5c). Similar to $NiSe_2$, the most Ni-rich phase among this thiospinel series ($CuCo_{0.8}Ni_{1.2}S_4$) shows the least decrease in H_2O_2 selectivity with increasing overpotential. These examples reveal the power of unveiling catalyst design principles via systematically modifying the compositions of well-defined crystal structures.

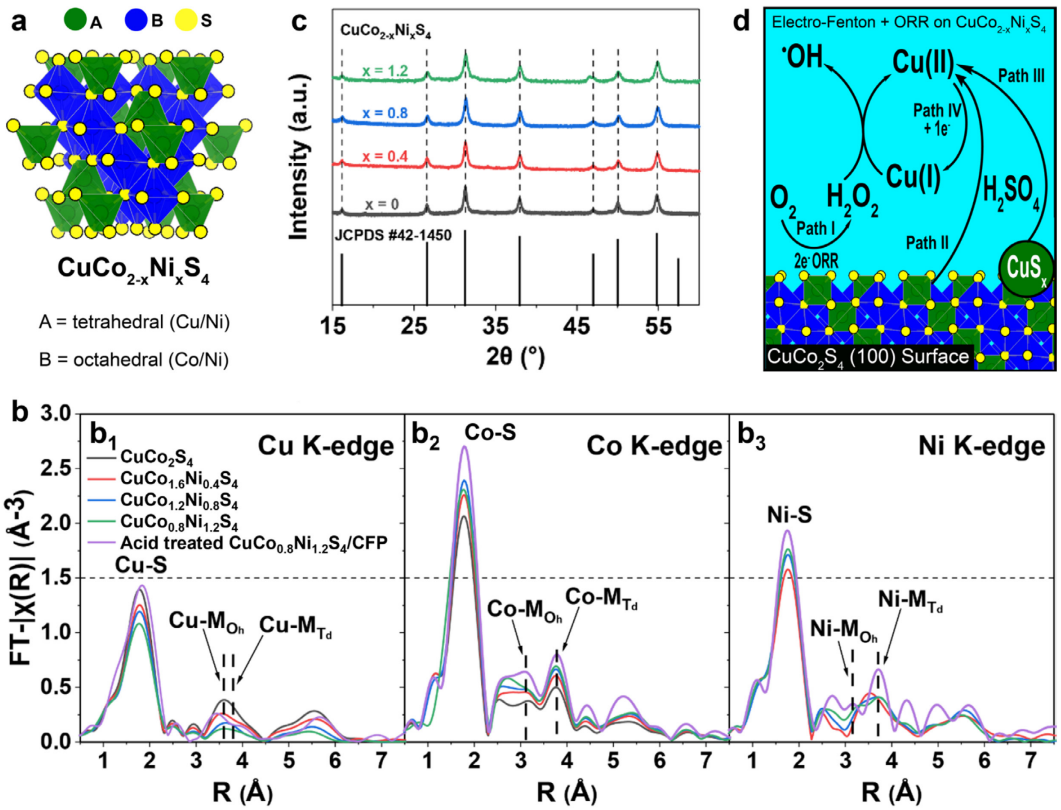

Figure 5. Structural characterizations of the thiospinel electrocatalysts. (a) Crystal structure of $CuCo_{2-x}Ni_xS_4$ thiospinels that exhibit mixed metal coordination environments (tetrahedral Cu and Ni sites; octahedral Co and Ni sites). (b) Extended X-ray absorption fine structures recorded at (b_1) Cu K-edge, (b_2) Co K-edge, and (b_3) Ni K-edge for as-synthesized $CuCo_{2-x}Ni_xS_4$ ($0 \leq x \leq 1.2$) catalysts and acid treated $CuCo_{0.8}Ni_{1.2}S_4$ catalyst grown on carbon fiber paper (CFP), showing scattering paths for the first shell (metal-sulfur) and the second shell (metal-metal, where M_{Td} and M_{Oh} stand for tetrahedral and octahedral metal sites, respectively). (c) Powder X-ray diffraction patterns of as-synthesized $CuCo_{2-x}Ni_xS_4$ ($0 \leq x \leq 1.2$) catalysts. (d) In competition with $2e^-$ ORR (Path I), as-synthesized $CuCo_{2-x}Ni_xS_4$ catalysts can readily leach copper species (Path II, III) that decompose the produced H_2O_2 and prevents H_2O_2 accumulation (Path IV), therefore pre-treatment of catalyst in acid is essential to enable practical H_2O_2 accumulation. Reprinted from ref. [25]. Copyright 2021 American Chemical Society.

Comparison of Kinetic Current Density for H_2O_2 Production. To quantitatively compare the $2e^-$ ORR catalyst performances from RRDE experiments, kinetic current density for H_2O_2 production ($j_{k,peroxide}$) can be derived by correcting the partial current density for H_2O_2 production ($j_{peroxide} = \frac{i_{ring}}{N \times A_{disk}}$, where A_{disk} is the geometric area of the disk) for mass-transport loss: $j_{k,peroxide} = (\frac{1}{j_{peroxide}} - \frac{1}{j_{L,peroxide}})^{-1}$, where $j_{L,peroxide}$ is the diffusion-limited current density for H_2O_2 production (~3 mA cm^{-2}_{disk} at 1600 rpm in O_2-saturated dilute aqueous solutions[22, 23]). We note that $j_{k,peroxide}$ is normalized by A_{disk} (mA cm^{-2}_{disk}) and reflects overall electrode performance rather than intrinsic catalytic property. An alternative term is mass activity for H_2O_2 production normalized by catalyst mass (mA $g^{-1}_{catalyst}$), but mass activity can vary with the specific surface area of a sample for different catalysts or even for different morphologies of the same catalyst. Additionally, the H_2O_2 selectivity can also be influenced by catalyst mass loading (see the section above). Therefore, $j_{k,peroxide}$ normalized by A_{disk} has practical merit from the point of view of end applications.

Figure 4c summarizes $j_{k,peroxide}$ achieved by many recently reported $2e^-$ ORR catalysts from RRDE experiments at 1600 rpm under O_2-saturated condition, with a specific focus on *acidic solution* and metal compound-based catalysts, including binary metal dichalcogenides[22-24] and quaternary thiospinels,[25] and other metal compounds[26, 27, 30-33, 48] with their crystal structures shown in Figure 6. In the low overpotential region, Co-based dichalcogenides[22, 23] show clearly more efficient H_2O_2 production than single-atom[19, 20, 49-52] or carbon[14, 15] catalysts, and display comparable or even better overall electrode performances than the state-of-the-art noble metal alloys.[11-13] Noble metal compounds such as PtP_2[26] and Pd_4Se[27] (their structures shown in Figure

6) eliminate the use of toxic Hg, yet can deliver comparable or higher $j_{k,peroxide}$ than Pt-Hg[11] and Pd-Hg[12] alloys. These encouraging results show the promise of metal compounds as high-performance acidic $2e^-$ ORR catalysts. However, many metal compounds exhibit decreasing H_2O_2 selectivity with increasing overpotential (see the section above), which prevents them from achieving high $j_{k,peroxide}$ at large overpotentials (see curvatures in Figure 4c) and restrict their use in efficient H_2O_2 production to the low overpotential region with limited current density. Therefore, future studies should focus on developing metal compound-based $2e^-$ ORR catalysts that are not only highly active but also highly selective up to large overpotentials to achieve high $j_{k,peroxide}$ for practical high-rate H_2O_2 production at large current densities.

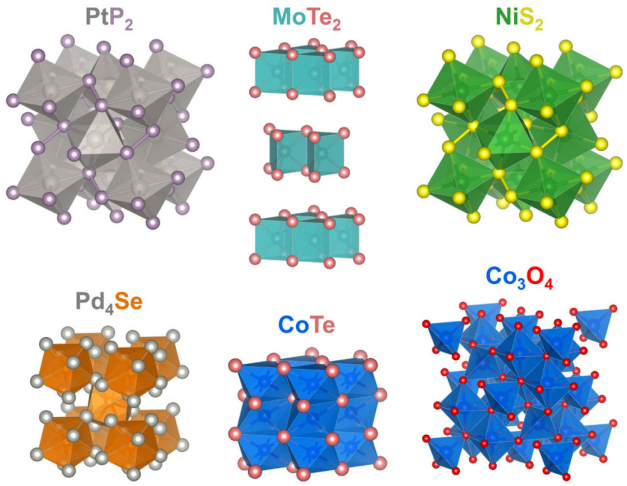

Figure 6. Crystal structures of other reported metal compounds that have been experimentally tested for $2e^-$ ORR in acidic solution (see detailed electrode information in Table S1), including PtP_2 (ref. [26]), Pd_4Se (ref. [27]), $MoTe_2$ (ref. [30]), CoTe (ref. [31]), NiS_2 (ref. [32]), and Co_3O_4 (ref. [33]). Their kinetic current densities for H_2O_2 production ($j_{k,peroxide}$) in acidic solution are shown in Figure 4c together with other catalysts. Note that PtP_2 (ref. [26]) and Pd_4Se (ref. [27]) are also

experimentally tested for $2e^-$ ORR in neutral solution (see detailed electrode information in Table S2, and their $j_{k,peroxide}$ in neutral solution shown in Figure S1).

Such comparisons of $j_{k,peroxide}$ also make it clear that there is more need for developing high-performance $2e^-$ ORR catalysts in acidic and neutral solutions (as opposed to alkaline solution). In addition to Figure 4 that compares $j_{k,peroxide}$ of reported $2e^-$ ORR catalysts in acidic solutions, Figure S1 and S2 summarize $j_{k,peroxide}$ achieved by reported neutral and alkaline $2e^-$ ORR catalysts, respectively. There exist much fewer examples of neutral $2e^-$ ORR catalysts (Figure S1), and many of them were tested in unbuffered neutral solutions where the alkaline shift of local pH near the electrode during ORR operation could give an inaccurate depiction of neutral $2e^-$ ORR catalytic properties. The $CoSe_2$ polymorph catalysts[23] (tested in neutral phosphate buffer) and other reported noble metal compounds (PtP_2[26] and Pd_4Se[27]) also clearly show higher $j_{k,peroxide}$ than single-atom[17, 18] and carbon[14, 15] catalysts under neutral conditions (Figure S1). On the other hand, the cost-effective carbon materials show very efficient H_2O_2 production at alkaline pH compared to other classes of catalysts (Figure S2), therefore the need for developing new alkaline $2e^-$ ORR catalysts is less urgent.

Catalyst Stability and Monitoring of Catalyst Leaching. Because of the corrosive acidic solution and the oxidizing environment involving the O_2 reactant and H_2O_2 product, it is crucial to use quantitative metrics to rigorously characterize the stability of acidic (and neutral) $2e^-$ ORR catalysts. Long-term RRDE stability tests of binary metal dichalcogenide catalysts were performed by continuously applying LSV scans on the disk,[22-24] similar to the typical accelerated

degradation tests for $4e^-$ ORR catalysts.[53] By monitoring the disk current and ring current at a fixed potential of 0.5 V vs. RHE, the catalyst stability follows the trend of *c*-$NiSe_2$ > (*c*-$CoSe_2$ ≈ *o*-$CoSe_2$) > *c*-CoS_2 in O_2-saturated 0.05 M H_2SO_4 (Figure 4d), in agreement with the stability computationally predicted based on surface adsorbate analyses (Figure 3b). The spent catalysts from RRDE experiments were routinely recovered to examine their surface and bulk structural stability by X-ray photoelectron spectroscopy (XPS) and Raman spectroscopy.[22-24]

The leaching of catalytic active elements is a major cause of electrocatalyst instability and can be quantified by elemental analyses of spent electrolytes using inductively coupled plasma mass spectrometry (ICP-MS). Catalyst leaching-based metrics have been introduced for evaluating the stability of acidic OER catalysts in terms of stability number;[54] however, catalyst leaching monitoring has been rarely performed in the studies of $2e^-$ ORR catalysts so far. Minimizing metal leaching is also crucial to direct utilization of $2e^-$ ORR electrocatalysis in water treatment applications without the need for further treatment steps to eliminate toxic elements to meet water safety regulations. For example, Pt-Hg alloy was found to experience severe leaching of toxic Hg, at a rate three orders of magnitude higher than the leaching of Pt, under potentiostatic operation at 0.5 V vs. RHE in O_2-saturated 0.1 M $HClO_4$ (Figure 7a, left), thus hindering the practical application of Pt-Hg catalyst. In comparison, PtP_2 showed greatly reduced leaching of heavy metals under the same conditions (Figure 7a, right), but it still experienced substantial loss in activity over time due to catalyst leaching and nanoparticle aggregation, and required an Al_2O_3 overcoat for stabilization (Figure 7b).[26]

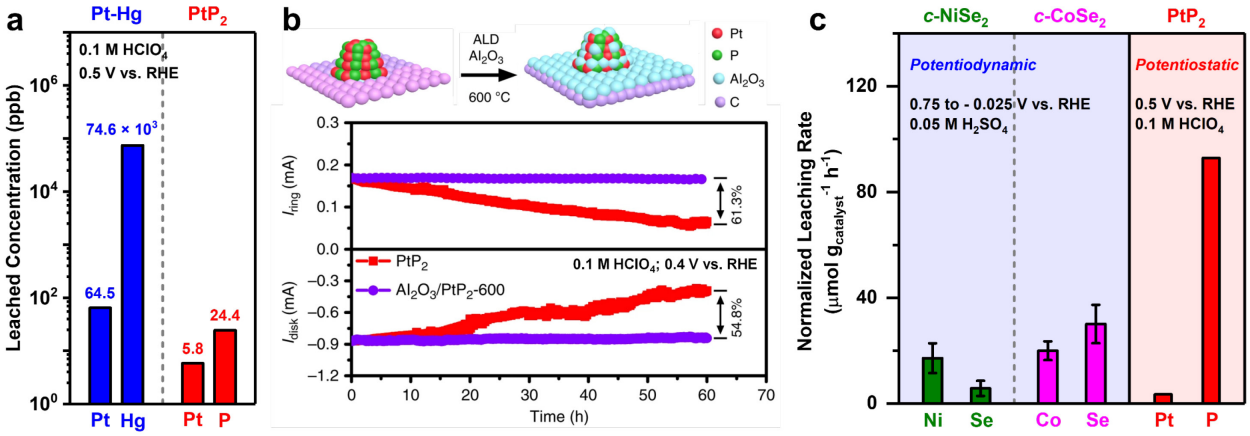

Figure 7. Monitoring the elemental leaching of metal compound-based 2e$^-$ ORR catalysts. (a) The concentrations of leached elements from Pt-Hg vs. PtP_2 (catalyst loading is 0.2 $mg_{catalyst}$ cm^{-2}_{disk} for both) after operating at 0.5 V vs. RHE in O_2-saturated 0.1 M $hClO_4$ (40 mL) for 6 hours. Source data are adapted from ref. [26]. (b) The activity loss of PtP_2 during RRDE testing, and its stabilization by an Al_2O_3 overcoat. Reprinted from ref. [26]. CC-BY-4.0 (https://creativecommons.org/licenses/by/4.0/). Copyright 2020 Springer Nature Limited. (c) The normalized leaching rates of metal and nonmetal elements (μmol $g_{catalyst}^{-1}$ h^{-1}) of *c*-$NiSe_2$ and *c*-$CoSe_2$ after long-term RRDE stability tests in acidic solution in comparison with PtP_2. Source data for *c*-$NiSe_2$ and *c*-$CoSe_2$ in panel (c) are adapted from ref. [24]. Copyright 2022 Springer Nature Limited. Source data for PtP_2 in panel (c) are adapted and converted from ref. [26] for comparison.

We have carefully monitored catalyst leaching of metal chalcogenide-based acidic 2e$^-$ ORR catalysts to benchmark their stability.[22-25] Figure 7c shows the direct comparisons of the metal and selenium leaching rates, normalized by the catalyst masses (μmol $g_{catalyst}^{-1}$ h^{-1}), of *c*-$NiSe_2$ and *c*-$CoSe_2$ catalysts during long-term RRDE stability tests in O_2-saturated 0.05 M H_2SO_4. The ratio between the Co and Se leaching rates of $CoSe_2$ is close to the 1:2 stoichiometry

(Figure 7c, middle). This suggests the leaching of $CoSe_2$ could be initiated by the surface oxidation of Se_2^{2-} to the readily soluble SeO_x due to the preferential affinity of O* to its Se site (see Figure 3b), followed by the near-stoichiometric dissolution of Co^{2+} from the surface. In contrast, the Se leaching from the more stable $NiSe_2$ is not only much more suppressed compared to $CoSe_2$, but also slower than the Ni leaching (Figure 7c, left). These suggest the leaching of $NiSe_2$ could mainly result from the preferential adsorption of O* and OH* to its Ni site (see Figure 3b) and the subsequent acid-base reaction with the electrolyte to dissolve Ni^{2+}. Future studies will help to confirm the catalyst leaching mechanisms of $NiSe_2$ vs. $CoSe_2$ (see below). We note that PtP_2 exhibits a much faster anion leaching (Figure 7c, right) than $NiSe_2$ and $CoSe_2$, yet the slower Pt metal leaching may be a potential advantage of noble metal compounds compared to earth-abundant metal compounds.

Since electrocatalyst leaching can closely depend on operating conditions such as applied potential,[54] future studies of $2e^-$ ORR catalysts may utilize *in situ* or *operando* techniques for real-time detection of dissolved species. *In situ* ICP-MS technique using a stationary probe near rotating disk electrode (SPRDE-ICPMS)[55] has been implemented for real-time elucidation of the potential-dependent dissolutions of OER[56] and $4e^-$ ORR[57] catalysts. In addition, electrochemical quartz crystal microbalance (EQCM)[58] can also probe the dissolutions of electrocatalysts in real time by tracking their mass changes as a function of potential.[21] These techniques will provide in-depth understanding and more guidance for developing more stable metal compound-based $2e^-$ ORR catalysts in the future.

Faradaic Side Reaction of H_2O_2 Electroreduction and Its Impact on H_2O_2 Accumulation. RRDE only provides instantaneous detection of H_2O_2 transiently produced by

$2e^-$ ORR catalysts, with negligible H_2O_2 concentration in the bulk solution. The produced H_2O_2 can be further electrochemically reduced to water ($H_2O_2 + 2\ H^+ + 2\ e^- \rightarrow 2\ H_2O$, $E^o = 1.76$ V vs. RHE), which is thermodynamically more favorable than $2e^-$ ORR. To ensure that the produced H_2O_2 can accumulate in the bulk solution and reach practically useful concentrations, it is critical to evaluate the peroxide reduction reaction (PRR) as a possible Faradaic side reaction, which has rarely been investigated in the recent $2e^-$ ORR studies.[24, 51, 52] PRR can be studied in Ar-saturated H_2O_2-containing solution using the catalyst-coated RRDE by only connecting the disk to the three-electrode cell. The same RRDE tested for $2e^-$ ORR in O_2-saturated H_2O_2-free solution can be reused to ensure the same catalyst loading and head-to-head comparisons of PRR vs. $2e^-$ ORR.

Recently performed systematic RRDE studies of PRR on *c*-$NiSe_2$ and *c*-$CoSe_2$ catalysts in acidic solutions[24] show that PRR and $2e^-$ ORR on *c*-$NiSe_2$ exhibit similar catalytic onset potentials and the rate of PRR increases with higher overpotential and H_2O_2 concentration (Figure 8a). The rates of PRR and $2e^-$ ORR are described by current densities: $j_{\mathrm{PRR}} = \frac{i_{\mathrm{PRR}}}{A_{\mathrm{disk}}}$, and $j_{\mathrm{peroxide}} = \frac{i_{\mathrm{ring}}}{N \times A_{\mathrm{disk}}}$ (vide supra). At nontrivial H_2O_2 concentration, the net rate of H_2O_2 production should correlate to $j_{\mathrm{peroxide}} - j_{\mathrm{PRR}}$, which remains positive only in a certain potential range and displays a parabolic trend peaking at an optimum potential (Figure 8b). Comparatively, the net rate of H_2O_2 production on *c*-$CoSe_2$ is less affected by PRR at low overpotentials as it exhibits a more positive catalytic onset potential for $2e^-$ ORR (Figure 8a and $4a_1$). Understanding PRR is informative for identifying the optimal operating conditions for bulk electrosynthesis of H_2O_2 (see the section below). Furthermore, it is important to investigate the mechanism of PRR[59] and

the ways to suppress it, which would lead to better-performing metal compound-based 2e$^-$ ORR catalysts for practical H_2O_2 electrosynthesis.

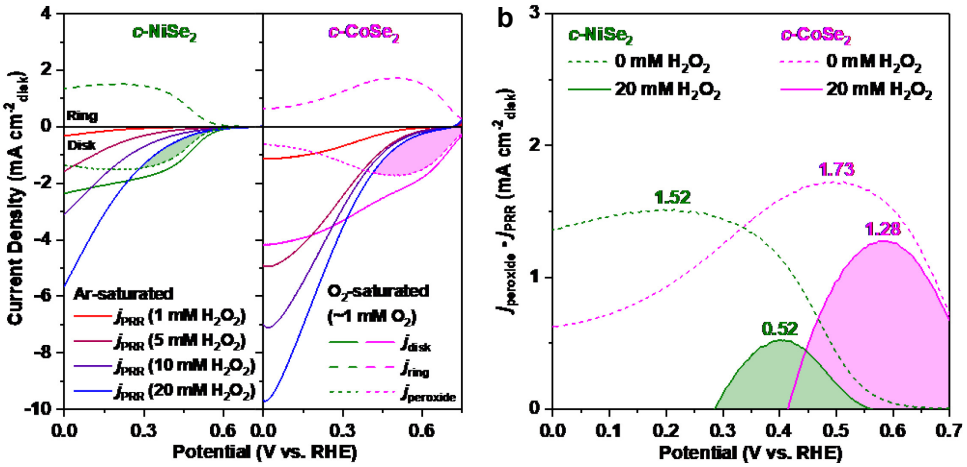

Figure 8. RRDE studies of peroxide reduction reaction (PRR) on *c*-$NiSe_2$ and *c*-$CoSe_2$ 2e$^-$ ORR catalysts. (a) Disk current densities (j_{disk}), ring current densities (j_{ring}), and partial current densities for H_2O_2 production ($j_{peroxide}$) of *c*-$NiSe_2$ and *c*-$CoSe_2$ catalysts at 1600 rpm in O_2-saturated 0.05 M H_2SO_4, in comparison with PRR current densities (j_{PRR}) at 1600 rpm in Ar-saturated 0.05 M H_2SO_4 containing 1, 5, 10, or 20 mM H_2O_2. (b) Net rates of H_2O_2 production on *c*-$NiSe_2$ and *c*-$CoSe_2$ catalysts are expected to correlate to $j_{peroxide} - j_{PRR}$. Reprinted from ref. [24]. Copyright 2022 Springer Nature Limited.

Bulk Electrosynthesis and Accumulation of H_2O_2. Bulk electrosynthesis of H_2O_2 on metal compound-based 2e$^-$ ORR catalysts can typically be performed in a conventional H-cell where the produced H_2O_2 accumulates in the catholyte that is separated from the anolyte by a proton exchange membrane to avoid the oxidation of H_2O_2 at the anode (Figure 9a). The produced H_2O_2 can be chemically quantified by spectrophotometric or titration methods.[60] Nanostructured metal chalcogenide catalysts can be directly grown on high surface-area carbon

fiber paper (CFP) as the cathode with high mechanical stability, and H_2O_2 electrosynthesis was carried out in a small volume (3–5 mL) of catholyte based on two-fold considerations: (1) the rapid accumulation of H_2O_2 in a small solution volume allows evaluating the maximum achievable H_2O_2 concentrations by metal compound-based $2e^-$ ORR catalysts and whether they catalyze the undesired H_2O_2 electroreduction; (2) higher concentrations of H_2O_2 pose more stringent tests for the stability of the $2e^-$ ORR catalysts during H_2O_2 bulk electrosynthesis.

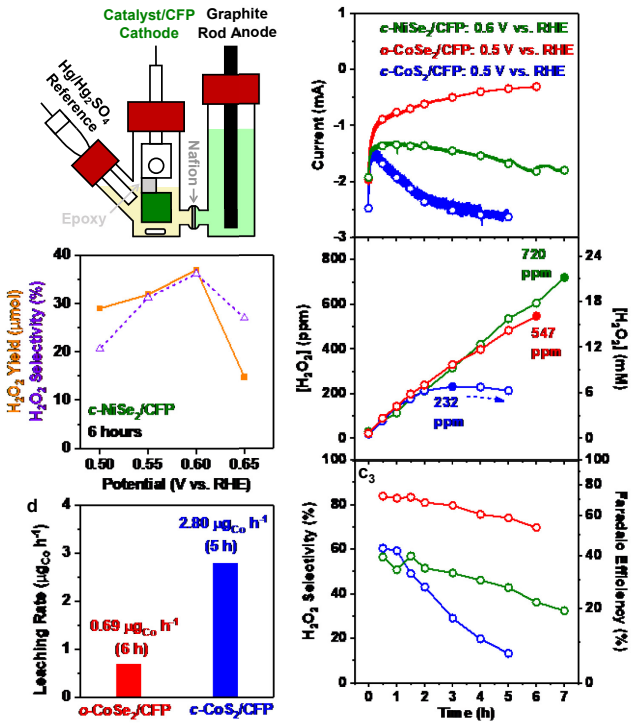

Figure 9. Bulk electrosynthesis of H_2O_2 on representative metal compound-based $2e^-$ ORR catalysts in the H-cell setup. (a) Schematic of three-electrode H-cell. (b) H_2O_2 yield and selectivity of *c*-$NiSe_2$/CFP (~1.06 μg_{Ni} cm^{-2}_{geo}, ~1 cm^2_{geo}) operated at different fixed applied potentials (0.50, 0.55, 0.60, or 0.65 V vs. RHE) for 6 h in O_2-saturated 0.05 M H_2SO_4 (4 mL, stirred at 1200 rpm). (c) H_2O_2 bulk electrosynthesis on *c*-CoS_2/CFP vs. *o*-$CoSe_2$/CFP vs. *c*-$NiSe_2$/CFP in 0.05 M H_2SO_4, where (c_1) shows steady-state current during chronoamperometry, (c_2) shows accumulated H_2O_2 concentration as function of time, and (c_3) shows cumulative H_2O_2

selectivity and Faradaic efficiency over time. (d) Metal leaching of *o*-$CoSe_2$/CFP vs. *c*-CoS_2/CFP (~0.37 mg_{Co} cm^{-2}_{geo} and ~1 cm^2_{geo} for both) in (c). Source picture in panel (a) is adapted from ref. [24]. Copyright 2022 Springer Nature Limited. Source data for *c*-CoS_2/CFP and *o*-$CoSe_2$/CFP in panels (c) and (d) are adapted from ref. [23]. Copyright 2020 Royal Society of Chemistry. Source data for *c*-$NiSe_2$/CFP in panels (b) and (c) are adapted from ref. [24]. Copyright 2022 Springer Nature Limited.

Both the cumulative H_2O_2 yield and selectivity from H_2O_2 bulk electrosynthesis on *c*-$NiSe_2$/CFP in O_2-saturated 0.05 M H_2SO_4 were found to be potential-dependent, and peaked at the optimum potential of 0.60 V vs. RHE (Figure 9b).[24] These observations were in agreement with RRDE studies of PRR where the net rate of H_2O_2 production on *c*-$NiSe_2$ displayed a parabolic trend as a function of potential in H_2O_2-containing solution (Figure 8b). Therefore, it is critical to operate H_2O_2 bulk electrosynthesis at the optimum potential to maximize H_2O_2 production and minimize the undesired H_2O_2 electroreduction. There is distinctive difference between the H_2O_2 bulk electrosynthesis performance among binary metal dichalcogenide catalysts (*c*-CoS_2 vs. *o*-$CoSe_2$ vs *c*-$NiSe_2$) in 0.05 M H_2SO_4 (Figure 9c).[23, 24] *c*-CoS_2 shows the most severe PRR side reaction, as evidenced by the increasing cathodic current over time (Figure 9c_1), and the H_2O_2 concentration only reached a maximum of 232 ppm and started decreasing afterwards (Figure 9c_2). In contrast, *o*-$CoSe_2$ is the least affected by PRR, achieving steadily increasing H_2O_2 concentration up to 547 ppm (Figure 9c_2) with the highest H_2O_2 selectivity among these three catalysts (Figure 9c_3). *c*-$NiSe_2$ exhibits a moderate H_2O_2 selectivity for bulk electrosynthesis (Figure 9c_3) likely because it is more affected by PRR than $CoSe_2$ (see Figure 8b), but *c*-$NiSe_2$ can still achieve steady accumulation of H_2O_2 up to a higher concentration of

720 ppm (Figure 9c$_2$). These varied results of bulk electrosynthesis on the series of binary metal chalcogenide catalysts further illustrate the complex interplay of various factors ($2e^-$ ORR catalytic activity, selectivity, stability, and electroreduction of H_2O_2) for realizing high practical performance of H_2O_2 electrosynthesis.

Monitoring and suppression of the undesired metal leaching and H_2O_2 electroreduction side reaction are crucial for successful H_2O_2 bulk electrosynthesis on metal compound-based $2e^-$ ORR catalysts. This is not only because the accumulated H_2O_2 is more demanding for catalyst stability than RRDE conditions (vide supra), but also because certain metal cations (Co^{3+}/Co^{2+}, Cu^{2+}/Cu^{+}, etc.) may chemically decompose the produced H_2O_2 (similar to the Fe^{2+}-mediated Fenton reaction).[29] For example, the leaching of Co^{2+} from *o*-$CoSe_2$ during H_2O_2 bulk electrosynthesis was clearly much slower than that from *c*-CoS_2 (Figure 9d),[23] which may also contribute to *o*-$CoSe_2$'s high H_2O_2 selectivity (Figure 9c$_3$).

As another interesting and more complex example, copper species can be readily leached from as-synthesized $CuCo_{2-x}Ni_xS_4$ thiospinel catalysts (Figure 5a). Such soluble Cu ions can prevent H_2O_2 accumulation because they can mediate the electro-Fenton process to decompose the produced H_2O_2 and generate ·OH (Figure 5d). Although RRDE tests showed the substitution of Ni for Co in $CuCo_{2-x}Ni_xS_4$ thiospinel structure enhances acidic $2e^-$ ORR (Figure 4a$_2$), bulk electrosynthesis using as-synthesized $CuCo_{0.8}Ni_{1.2}S_4$ catalyst (most Ni-rich) showed undetectable H_2O_2 accumulation during initial testing. However, H_2O_2 could be built up when the spent $CuCo_{0.8}Ni_{1.2}S_4$ catalyst was re-tested in a fresh acidic solution. Post-characterization revealed that ~50% of Cu in as-synthesized $CuCo_{0.8}Ni_{1.2}S_4$ was leached into electrolyte during initial testing, resulting in some rearrangement of the mixed metal coordination environments, but the bulk thiospinel structure was still maintained (Figure 5b). In contrast, Cu leaching was much less

pronounced during re-testing, suggesting that the enhanced stability of the spent $CuCo_{0.8}Ni_{1.2}S_4$ catalyst was key for successful H_2O_2 accumulation. Such initial Cu leaching and structural changes of as-synthesized $CuCo_{0.8}Ni_{1.2}S_4$, which could also be accomplished by a simple acid treatment without applying potential, was essential to condition the catalyst and enable practical H_2O_2 accumulation.[25] These results further highlight the need for ICP elemental analysis of the electrolyte tested for H_2O_2 bulk electrosynthesis, in addition to careful structural characterization of the spent catalysts.

Device Engineering for Practical Electrosynthesis of H_2O_2

While an H-cell offers a simple setup for small-scale H_2O_2 electrosynthesis, it suffers from several drawbacks including low solubility of O_2 in the liquid phase, limited diffusion of O_2 to the catalyst, and high local concentration of H_2O_2 near the cathode, all of which hinder the production rate, concentration, and selectivity. These can be overcome by careful electrochemical device engineering.[61-64] The O_2 solubility and diffusion limitations can primarily be addressed by the use of catalyst-loaded hydrophobic gas diffusion electrodes (GDEs) and flow cells to deliver constant flow of O_2 gas directly to the catalyst surface at the three-phase boundary. Such benefits of the engineered electrochemical devices, which have been well studied for water splitting electrolyzers[65] and CO_2 electroreduction devices,[66] are starting to be exploited for practical electrosynthesis of H_2O_2.[61-64]

In a recent work, a GDE coated with a layer-templated $CoSe_2$ (sc-$CoSe_2$) catalyst was run in a flow cell (Figure 10a) and achieved a large H_2O_2 partial current density up to 60 mA cm^{-2} (Figure 10b) for high-rate and selective H_2O_2 production in recirculated 0.5 M H_2SO_4.[48] The sc-$CoSe_2$ GDE showed 100 hours of stable continuous operation at 63 mA cm^{-2} with >90% Faradaic

efficiency toward H_2O_2 (Figure 10c), but the electrolyte was replaced with fresh electrolyte every hour with ~1900 ppm H_2O_2 produced, so the maximum achievable H_2O_2 concentration by the GDE was not approached. Another recent work operated a PtP_2 GDE in a PEM fuel cell (Figure 10d) and reached an impressive high concentration plateau of ~40,000 ppm H_2O_2 (~4 wt%) in a large volume (600 mL) of continuously recycled neutral water flow (Figure 10e), whereas only ~500 ppm was accumulated without recycling water (Figure 10e inset).[26] It was also necessary to optimize other conditions to maximize H_2O_2 accumulation, such as the hydrophobicity of GDE to avoid cathode flooding, and the catalyst loading, water flow rate, and temperature to minimize H_2O_2 degradation. Furthermore, the interfacial electrolyte can also affect H_2O_2 electrosynthesis in flow cells. A recent report showed that adding a small amount of alkali metal ions into aqueous protic electrolytes greatly enhances the Faradaic efficiency toward H_2O_2 on carbon GDEs, as these metal ions could shield H^+ from the electrode/electrolyte interface and suppress the undesired H_2O_2 electroreduction to water.[67] These results show the promise of scaling up H_2O_2 electrosynthesis using metal compound-based $2e^-$ ORR catalysts in well-engineered devices to achieve high practical performance.

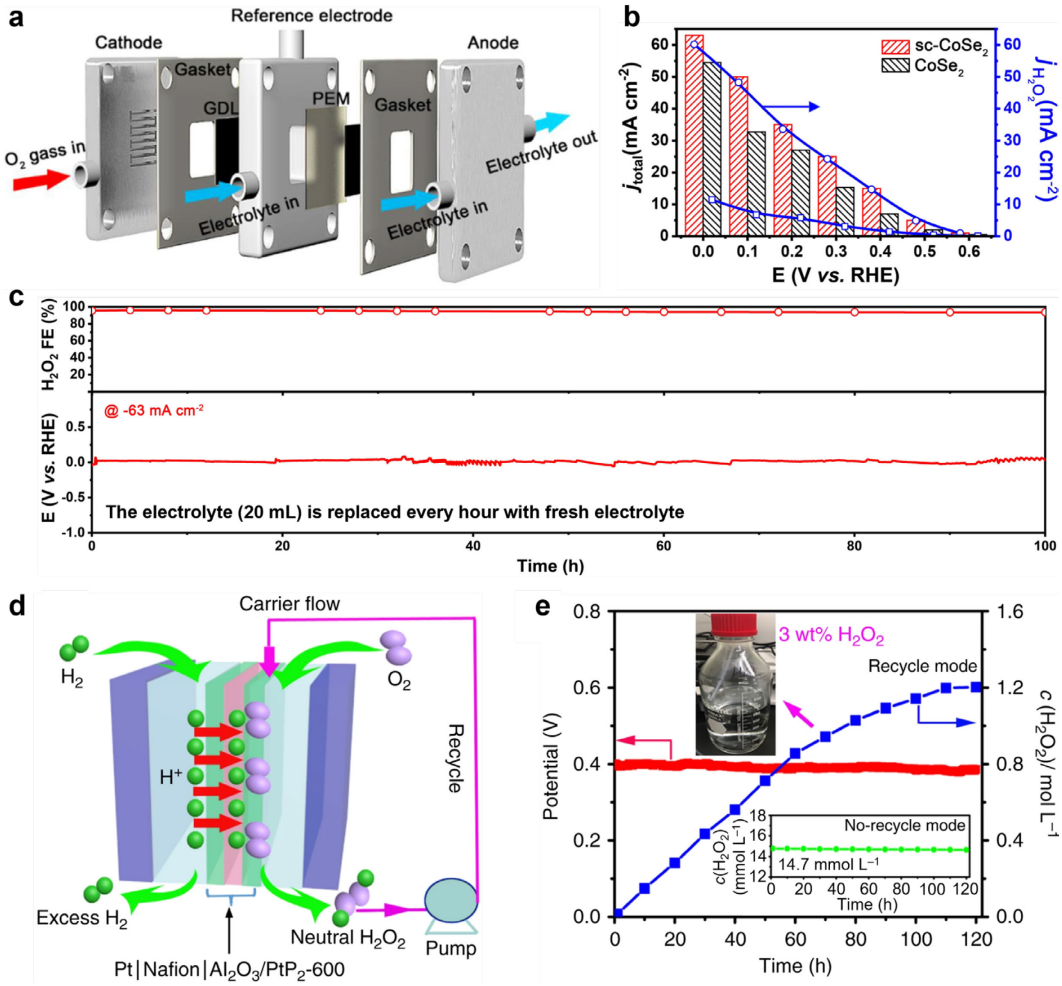

Figure 10. Bulk electrosynthesis of H_2O_2 on metal compound-based $2e^-$ ORR catalysts in flow cells. (a) Schematic of a flow electrolyzer using a GDE cathode coated with a layer-templated sc-$CoSe_2$ catalyst. (b) Total current density and H_2O_2 partial current density of the sc-$CoSe_2$ GDE (in comparison to the GDE coated with a bulk $CoSe_2$ catalyst). (c) Continuous operation of the sc-$CoSe_2$ GDE. (d) Schematic of a PEM fuel cell using a GDE cathode coated with a PtP_2 catalyst for H_2O_2 electrosynthesis. (e) H_2O_2 accumulation to a high concentration plateau in neutral water by recycling the water flow vs. the much lower steady-state concentration without recycling the water flow as shown in the inset. Panels (a)–(c) are reprinted from ref. [48]. Copyright 2021 Wiley-VCH Verlag GmbH & Co. Panels (d) and (e) are reprinted from ref. [26].

Importantly, for benchmarking the performances of these GDEs, the cell configurations and device operating conditions must be accurately reported.[68] Additionally, electrode preparation methods should be carefully described, as the catalyst microstructure can affect the diffusion of O_2 and H_2O_2 in and out of the electrode,[69, 70] which can further impact the ability for H_2O_2 to accumulate and the Faradaic efficiency. Some factors to consider include the catalyst ink compositions (solvents, ionomers, catalyst concentrations),[71, 72] the properties of the electrode substrates (hydrophobicity, porosity),[73, 74] and the methods of depositing catalyst onto the electrodes (drop-casting,[21] spray coating,[74-76] or direct growth[22-25]). Because the many factors at the device, electrode, and catalyst level can impact the overall electrosynthesis performance, comparing the apparent H_2O_2 electrosynthesis performances under different cell conditions can further obfuscate atomic-level insights into the structural design of metal compound-based $2e^-$ ORR catalysts.

Electro-Fenton Process Enabled by Metal Compound-Based $2e^-$ ORR Catalysts

In addition to the common applications of H_2O_2 as an oxidant and disinfectant discussed in the introduction, the development of selective, active, and stable metal compound based $2e^-$ ORR catalysts in acidic solutions open up many new applications for the electrochemically produced H_2O_2 via the electro-Fenton process.

Environmental Remediation. The electro-Fenton process is useful for environmental remediation as it converts the electrogenerated H_2O_2 (E^o = 1.76 V vs. RHE) to the more

oxidizing ·OH (E^o = 2.80 V vs. RHE). This process occurs via Fe^{2+} mediation at the optimum pH of ~3 ($Fe^{2+} + H_2O_2 + H^+ \rightarrow Fe^{3+} + H_2O + \cdot OH$), where Fe^{2+} is regenerated at the cathode ($Fe^{3+} + e^- \rightarrow Fe^{2+}$) to accelerate the ·OH production.[29] The pH requirement of the electro-Fenton process can take advantage of the acidic $2e^-$ ORR catalysts based on metal compounds. The electro-Fenton process also is more demanding on the cathode stability than $2e^-$ ORR because ·OH is more oxidizing than H_2O_2. Considering the significantly enhanced catalyst stability and acidic H_2O_2 bulk electrosynthesis performance of $CoSe_2$ over CoS_2 (see Figure 4d and 7c), we used the $CoSe_2$ cathode to demonstrate the effective electro-Fenton degradation of rhodamine B (RhB), a model organic pollutant (Figure 11a).[23] More reports have recently appeared to use metal compounds such as CoS_2[77] and CoSP[78] for similar electro-Fenton removal of organic pollutants. The electro-Fenton process can also be mediated by other metal ions such as Cu^{2+}/Cu^+.[29] These soluble metal ions do not necessarily need to be added into the solution on purpose, but can come from metal leaching of the $2e^-$ ORR cathode itself, as discussed earlier that leached Cu species from as-synthesized $CuCo_{0.8}Ni_{1.2}S_4$ thiospinel cathode could trigger a built-in Cu-based electro-Fenton process (Figure 5d).[25] We note that such metal leaching could be a double-edged sword, as it could effectively contribute to ·OH formation but may also lead to cathode degradation. Future studies should not only carefully examine the stability of metal compound-based $2e^-$ ORR catalysts during electro-Fenton operations, but also could expand the applications based on such streamlined electro-Fenton process to other environmental challenges such as isolating microplastics from wastewater[79, 80] and separating plastic mixtures.[81]

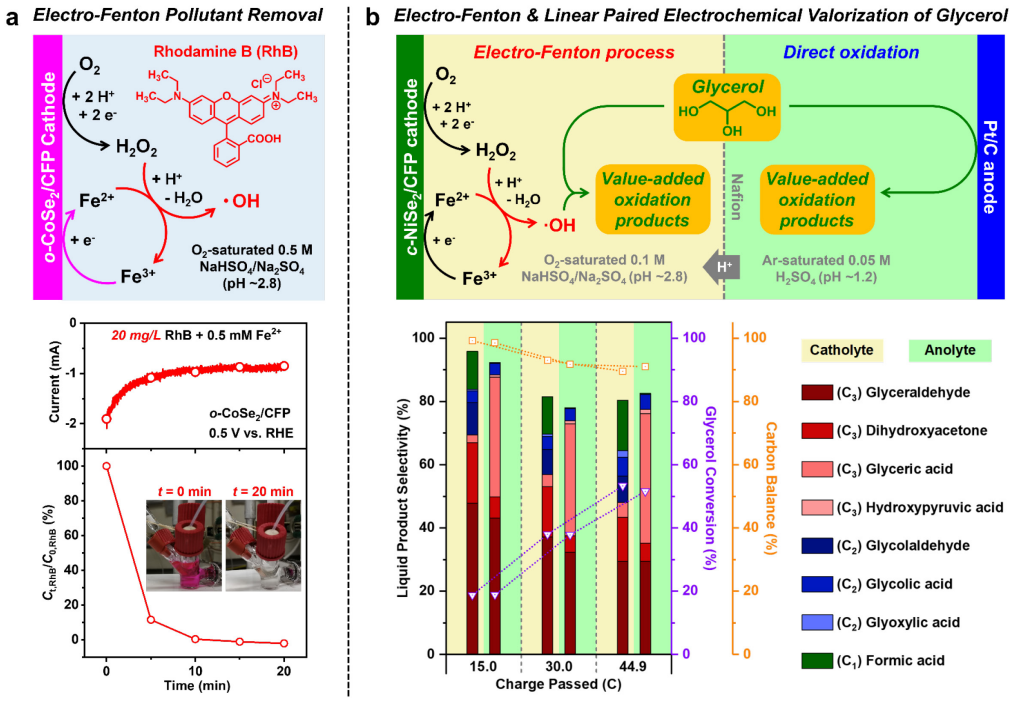

Figure 11. Using new metal compound-based 2e$^-$ ORR catalysts to enable the electro-Fenton process for environmental and biomass valorization applications. (a) Scheme of the electro-Fenton process, and the effective electro-Fenton degradation of rhodamine B (RhB) at *o*-$CoSe_2$ cathode. Reprinted from ref. [23]. Copyright 2020 Royal Society of Chemistry. (b) Scheme of linear paired electrochemical valorization of glycerol into the same oxidation products via the electro-Fenton process at the stable $NiSe_2$ cathode and via anodic oxidation at Pt anode simultaneously, with high glycerol conversion and high selectivity for value-added C_3 products achieved. Reprinted from ref. [24]. Copyright 2022 Springer Nature Limited.

Biomass Valorization into Value-Added Chemicals. The deployment of the electro-Fenton process has been largely limited to environmental treatment,[29] which motivated us to explore the use of the electro-Fenton process for enabling valuable chemical transformations. For

example, oxidative upgrading of biomass-derived feedstocks typically occurs solely via anodic oxidation,[82] but the electro-Fenton process may uniquely enable such oxidation reactions in the cathodic half-cell due to the strong oxidizing power of ·OH. Chemically generated ·OH from H_2O_2 has found use in biomass-to-chemical conversion[83] such as carbohydrate oxidation and lignin depolymerization, but the electro-Fenton process is less developed for making high-value chemicals than these aforementioned chemical processes.

Recently, we utilized the electro-Fenton process at the stable $NiSe_2$ cathode to enable efficient cathodic valorization of glycerol to the desired value-added oxidation products (such as glyceraldehyde, dihydroxyacetone, and glyceric acid) for the first time.[24] This is made possible by the excellent stability of $NiSe_2$ against surface oxidative leaching (Figure 7c), which is crucial for enabling long-term sustained electro-Fenton process because ·OH is very strongly oxidizing. In addition, it is critical to carefully optimize the Fe^{2+} concentration and the ·OH generation rate of the electro-Fenton process, so that high glycerol conversion and high selectivity for value-added C_3 and C_2 products can be concurrently achieved, and over-oxidation to C_1 or CO_2 products can be minimized. More importantly, the cathodic valorization of glycerol can be linear paired with anodic oxidation to produce the same oxidation products at both $NiSe_2$ cathode and Pt anode simultaneously, and achieve high glycerol conversion and high selectivity for value-added C_3 products, with less C_2 and C_1 products produced (Figure 11b). It is noteworthy that, after adjusting the supporting electrolyte condition, this linear paired system for concurrent valorization of glycerol (~50 mM) can operate at a very small external bias (<0.2 V) with little external energy input needed, which can theoretically be made into an unbiased system upon further optimization in the future. Further development and optimization of the linear paired process using electrochemical flow cells with catalyst loaded on GDEs (see the section above) or

PEM electrolyzers could further increase the production rates and yields and decrease the overall energy consumption. This novel use of the electro-Fenton process and this conceptual strategy of linear pairing the electro-Fenton process with anodic oxidation opens up new opportunities for enabling electrochemical valorization of diverse biomass-derived feedstocks[82] (5-hydroxymethylfurfural,[84] glucose,[85] glycerol,[86] etc.) with high atom efficiency and low energy cost.

To conclude, we have summarized the recently developed computational frameworks and experimental studies that led to the discovery of a series of new binary and quaternary metal chalcogenide and other metal compound catalysts for selective $2e^-$ ORR in acidic and neutral solutions. The new theoretical understanding provides guidance for rationally tailoring the crystal structures of metal compounds to enhance the $2e^-$ ORR selectivity and stability by suppressing the undesired O-O bond cleavage and surface oxidative degradation, respectively. Rigorous experimental monitoring of catalyst leaching and H_2O_2 electroreduction side reaction are critical for achieving significant improvements in both catalyst stability and H_2O_2 bulk electrosynthesis performance of metal chalcogenide-based $2e^-$ ORR catalysts. The electro-Fenton process on these robust and stable metal chalcogenide catalysts not only found use in environmental treatment, but also enabled the novel cathodic valorization and proof-of-concept linear paired electrochemical valorization of biomass-derived glycerol feedstock.

Careful survey of the current state-of-the-art in electrosynthesis of H_2O_2 shows that future developments of new $2e^-$ ORR catalysts should focus more on acidic and neutral conditions for which underexplored metal compound-based catalysts will find significant new opportunities. In addition to the binary metal dichalcogenides, phosphides, and occasional quaternary thiospinels discussed herein, there remain many metal compounds (such as metal pnictogenides, oxides,

carbides, borides, etc.) unexplored or underexplored for $2e^-$ ORR. For example, the Chevrel phases (general formula $M_xMo_6S_8$) possess high degrees of compositional flexibility for catalytic applications,[87] but they have only been briefly explored for $2e^-$ ORR in alkaline solution.[88] However, many studies of metal compound-based catalysts for $2e^-$ ORR so far were performed in alkaline solution, which is probably less productive, as carbon nanomaterials already perform quite well under alkaline conditions. Metal compounds such as chalcogenides and pnictogenides are also likely to be unstable chemically and electrochemically in strongly oxidizing alkaline solutions.[89] For example, from both Pourbaix and XPS analyses, CoS_2 is shown to form $Co(OH)_2$ and CoOOH (oxy)hydroxide phases on the surface at potentials relevant to $2e^-$ ORR under alkaline pH > 8.[46] Therefore, we strongly advocate for prioritizing the acidic and neutral conditions for future studies of metal compound-based $2e^-$ ORR catalysts, given the stability consideration and the already efficient alkaline $2e^-$ ORR on carbon nanomaterials.

Given that $2e^-$ ORR catalysts may exhibit pH-dependent catalytic properties, computational models can be insightful for elucidating such pH-dependence[90, 91] and identifying promising catalyst candidates for active and selective acidic and neutral $2e^-$ ORR. Moreover, the emerging computational approach of active motif screening[35] has led to high-throughput prediction of promising binary metal chalcogenide phases with expected high activity, selectivity, and stability for acidic or neutral $2e^-$ ORR. Such theoretical predictions should be experimentally explored, and this approach of active motif screening may be further developed for screening more complicated metal compounds. In addition, the recently demonstrated computational approach of combining the bulk Pourbaix stability from the Materials Project and the oxygen adsorbate energetics (or surface Pourbaix diagrams in general) from the Catalysis Hub for OER catalyst discovery[92] could also be used for screening metal compounds as $2e^-$ ORR

catalysts. To better understand the catalytic mechanisms and stability, *in situ* or *operando* techniques, such as X-ray absorption spectroscopy (XAS) and Raman spectroscopy, can be employed for probing the structural and electronic evolutions of the working catalysts.[21, 48] Moreover, *in situ* or *operando* attenuated total reflectance infrared spectroscopy (ATR-IR)[93] and ambient pressure XPS (APXPS)[94] can provide information about the catalyst/electrolyte interface by capturing key ORR adsorbates, which can further complement the computational modeling and achieve atomic-level mechanistic insights into catalyst design. The use of flow cells that build up practical concentrations of H_2O_2 (coupled with in-line detection of H_2O_2 and/or catalyst leaching) while measuring XAS at metal K-edges using hard X-rays or at metal L-edges (or K-edges/L-edges of the catalytic inert sites) using soft X-rays could further inform catalyst stability as well as active surface speciation in the working environment.

HIGHLIGHTED QUOTES

1. Metal compounds remain underexplored as $2e^-$ ORR catalysts for H_2O_2 electrosynthesis, but the mechanistic discussions suggest that metal compounds offer many exciting attributes for tailoring catalytic properties for $2e^-$ ORR.
2. General design principles for metal compound-based $2e^-$ ORR catalysts include optimizing OOH* adsorption for activity, kinetically suppressing O-O bond cleavage for selectivity, and destabilizing surface oxygen adsorbates for stability.
3. Monitoring and suppression of the undesired metal leaching and H_2O_2 electroreduction side reaction are crucial for successful H_2O_2 bulk electrosynthesis on metal compound-based $2e^-$ ORR catalysts.

4. We strongly advocate for prioritizing the acidic and neutral conditions for future studies of metal compound-based $2e^-$ ORR catalysts, given the stability consideration and the already efficient alkaline $2e^-$ ORR on carbon nanomaterials.

AUTHOR INFORMATION

Notes

A provisional patent has been filed by the authors (H.S., R.D.R, J.R.S, S.J.) based on some of their original research work summarized in this Focus Review.

Biographies

Hongyuan Sheng received his B.S. in chemistry from Fudan University in 2016 and Ph.D. in materials chemistry from the University of Wisconsin—Madison under the supervision of Professor Song Jin in 2022. He is currently conducting postdoctoral research with Professor Chong Liu at the University of California, Los Angeles. https://jin.chem.wisc.edu/content/hongyuan-sheng

R. Dominic Ross received his B.S. in chemistry from The Ohio State University in 2018 and is currently a Ph.D. candidate in materials chemistry under the supervision of Professor Song Jin at the University of Wisconsin—Madison. https://rdominicross.com/

J. R. Schmidt is a Professor of Chemistry at the University of Wisconsin—Madison and member of the Theoretical Chemistry Institute. He earned his B.S. from Hope College and Ph.D. from the University of Wisconsin—Madison. His research interests include developing accurate, first-principles force fields, nanoporous materials, and computational heterogeneous-/electro-catalysis. https://schmidt.chem.wisc.edu

Song Jin is the Francis J. DiSalvo Professor of Physical Science at the University of Wisconsin—Madison. He received his B.S. from Peking University and Ph.D. from Cornell University. He is interested in the chemistry, physics, and technological applications of nanoscale and solid-state materials, including electrocatalysis and renewable energy conversion. https://jin.chem.wisc.edu

SUPPORTING INFORMATION

The Supporting Information is available free of charge at the ACS website.

Additional comparisons of kinetic current densities for H_2O_2 production ($j_{k,peroxide}$) on different classes of $2e^-$ ORR catalysts in neutral (Figure S1) and alkaline (Figure S2) solutions. Detailed catalyst and electrode information for $j_{k,peroxide}$ comparisons (Tables S1–S3).

ACKNOWLEDGMENTS

This work is supported by the National Science Foundation (NSF) Grant CHE-1955074. The authors thank Dr. Eric D. Hermes, Dr. Aurora N. Janes, and Mr. Kwanpyung Lee who performed the computational studies of metal dichalcogenide-based $2e^-$ ORR catalysts summarized in this Focus Review.

REFERENCES

(1) Campos-Martin, J. M.; Blanco-Brieva, G.; Fierro, J. L. G., Hydrogen Peroxide Synthesis: An Outlook beyond the Anthraquinone Process. *Angew. Chem. Int. Ed.* **2006**, *45*, 6962-6984.

(2) Hydrogen Peroxide Market Share, Size, Trends, Industry Analysis Report, By Function (Disinfectant, Bleaching, Oxidant, Others); By Application; By Region; Segment Forecast, 2021 - 2028. https://www.researchandmarkets.com/reports/5459592/hydrogen-peroxide-market-share-size-trends (accessed July 14, 2022).

(3) Yang, S.; Verdaguer-Casadevall, A.; Arnarson, L.; Silvioli, L.; Čolić, V.; Frydendal, R.; Rossmeisl, J.; Chorkendorff, I.; Stephens, I. E. L., Toward the Decentralized Electrochemical Production of H_2O_2: A Focus on the Catalysis. *ACS Catal.* **2018**, *8*, 4064-4081.

(4) Jiang, Y.; Ni, P.; Chen, C.; Lu, Y.; Yang, P.; Kong, B.; Fisher, A.; Wang, X., Selective Electrochemical H_2O_2 Production through Two-Electron Oxygen Electrochemistry. *Adv. Energy Mater.* **2018**, *8*, 1801909.

(5) Perry, S. C.; Pangotra, D.; Vieira, L.; Csepei, L.-I.; Sieber, V.; Wang, L.; Ponce de León, C.; Walsh, F. C., Electrochemical Synthesis of Hydrogen Peroxide from Water and Oxygen. *Nat. Rev. Chem.* **2019**, *3*, 442-458.

(6) Siahrostami, S.; Villegas, S. J.; Bagherzadeh Mostaghimi, A. H.; Back, S.; Farimani, A. B.; Wang, H.; Persson, K. A.; Montoya, J., A Review on Challenges and Successes in Atomic-Scale Design of Catalysts for Electrochemical Synthesis of Hydrogen Peroxide. *ACS Catal.* **2020**, *10*, 7495-7511.

(7) Wang, F.; Li, W.; Wang, R.; Guo, T.; Sheng, H.; Fu, H.-C.; Stahl, S. S.; Jin, S., Modular Electrochemical Synthesis Using a Redox Reservoir Paired with Independent Half-Reactions. *Joule* **2021**, *5*, 149-165.

(8) Wang, R.; Sheng, H.; Wang, F.; Li, W.; Roberts, D. S.; Jin, S., Sustainable Coproduction of Two Disinfectants via Hydroxide-Balanced Modular Electrochemical Synthesis Using a Redox Reservoir. *ACS Cent. Sci.* **2021**, *7*, 2083-2091.

(9) Seh, Z. W.; Kibsgaard, J.; Dickens, C. F.; Chorkendorff, I.; Nørskov, J. K.; Jaramillo, T. F., Combining Theory and Experiment in Electrocatalysis: Insights into Materials Design. *Science* **2017**, *355*, eaad4998.

(10) Shi, X.; Back, S.; Gill, T. M.; Siahrostami, S.; Zheng, X., Electrochemical Synthesis of H_2O_2 by Two-Electron Water Oxidation Reaction. *Chem* **2021**, *7*, 38-63.

(11) Siahrostami, S.; Verdaguer-Casadevall, A.; Karamad, M.; Deiana, D.; Malacrida, P.; Wickman, B.; Escudero-Escribano, M.; Paoli, E. A.; Frydendal, R.; Hansen, T. W.; Chorkendorff, I.; Stephens, I. E. L.; Rossmeisl, J., Enabling Direct H_2O_2 Production through Rational Electrocatalyst Design. *Nat. Mater.* **2013**, *12*, 1137-1143.

(12) Verdaguer-Casadevall, A.; Deiana, D.; Karamad, M.; Siahrostami, S.; Malacrida, P.; Hansen, T. W.; Rossmeisl, J.; Chorkendorff, I.; Stephens, I. E. L., Trends in the Electrochemical Synthesis of H_2O_2: Enhancing Activity and Selectivity by Electrocatalytic Site Engineering. *Nano Lett.* **2014**, *14*, 1603-1608.

(13) Zhao, X.; Yang, H.; Xu, J.; Cheng, T.; Li, Y., Bimetallic PdAu Nanoframes for Electrochemical H_2O_2 Production in Acids. *ACS Mater. Lett.* **2021**, *3*, 996-1002.

(14) Lu, Z.; Chen, G.; Siahrostami, S.; Chen, Z.; Liu, K.; Xie, J.; Liao, L.; Wu, T.; Lin, D.; Liu, Y.; Jaramillo, T. F.; Nørskov, J. K.; Cui, Y., High-Efficiency Oxygen Reduction to Hydrogen Peroxide Catalysed by Oxidized Carbon Materials. *Nat. Catal.* **2018**, *1*, 156-162.

(15) Sun, Y.; Sinev, I.; Ju, W.; Bergmann, A.; Dresp, S.; Kühl, S.; Spöri, C.; Schmies, H.; Wang, H.; Bernsmeier, D.; Paul, B.; Schmack, R.; Kraehnert, R.; Roldan Cuenya, B.; Strasser, P., Efficient Electrochemical Hydrogen Peroxide Production from Molecular Oxygen on Nitrogen-Doped Mesoporous Carbon Catalysts. *ACS Catal.* **2018**, *8*, 2844-2856.

(16) Xia, C.; Xia, Y.; Zhu, P.; Fan, L.; Wang, H., Direct Electrosynthesis of Pure Aqueous H_2O_2 Solutions up to 20% by Weight Using a Solid Electrolyte. *Science* **2019**, *366*, 226-231.

(17) Sun, Y.; Silvioli, L.; Sahraie, N. R.; Ju, W.; Li, J.; Zitolo, A.; Li, S.; Bagger, A.; Arnarson, L.; Wang, X.; Moeller, T.; Bernsmeier, D.; Rossmeisl, J.; Jaouen, F.; Strasser, P., Activity–Selectivity Trends in the Electrochemical Production of Hydrogen Peroxide over Single-Site Metal–Nitrogen–Carbon Catalysts. *J. Am. Chem. Soc.* **2019**, *141*, 12372-12381.

(18) Jiang, K.; Back, S.; Akey, A. J.; Xia, C.; Hu, Y.; Liang, W.; Schaak, D.; Stavitski, E.; Nørskov, J. K.; Siahrostami, S.; Wang, H., Highly Selective Oxygen Reduction to Hydrogen Peroxide on Transition Metal Single Atom Coordination. *Nat. Commun.* **2019**, *10*, 3997.

(19) Gao, J.; Yang, H. b.; Huang, X.; Hung, S.-F.; Cai, W.; Jia, C.; Miao, S.; Chen, H. M.; Yang, X.; Huang, Y.; Zhang, T.; Liu, B., Enabling Direct H_2O_2 Production in Acidic Media through Rational Design of Transition Metal Single Atom Catalyst. *Chem* **2020**, *6*, 658-674.

(20) Shen, R.; Chen, W.; Peng, Q.; Lu, S.; Zheng, L.; Cao, X.; Wang, Y.; Zhu, W.; Zhang, J.; Zhuang, Z.; Chen, C.; Wang, D.; Li, Y., High-Concentration Single Atomic Pt Sites on Hollow CuS_x for Selective O_2 Reduction to H_2O_2 in Acid Solution. *Chem* **2019**, *5*, 2099-2110.

(21) Ross, R. D.; Sheng, H.; Ding, Y.; Janes, A. N.; Feng, D.; Schmidt, J. R.; Segre, C. U.; Jin, S., Operando Elucidation of Electrocatalytic and Redox Mechanisms on a 2D Metal Organic Framework Catalyst for Efficient Electrosynthesis of Hydrogen Peroxide in Neutral Media. *J. Am. Chem. Soc.* **2022**, DOI: 10.1021/jacs.2c06810.

(22) Sheng, H.; Hermes, E. D.; Yang, X.; Ying, D.; Janes, A. N.; Li, W.; Schmidt, J. R.; Jin, S., Electrocatalytic Production of H_2O_2 by Selective Oxygen Reduction Using Earth-Abundant Cobalt Pyrite (CoS_2). *ACS Catal.* **2019**, *9*, 8433-8442.

(23) Sheng, H.; Janes, A. N.; Ross, R. D.; Kaiman, D.; Huang, J.; Song, B.; Schmidt, J. R.; Jin, S., Stable and Selective Electrosynthesis of Hydrogen Peroxide and the Electro-Fenton Process on $CoSe_2$ Polymorph Catalysts. *Energy Environ. Sci.* **2020**, *13*, 4189-4203.

(24) Sheng, H.; Janes, A. N.; Ross, R. D.; Hofstetter, H.; Lee, K.; Schmidt, J. R.; Jin, S., Linear Paired Electrochemical Valorization of Glycerol Enabled by the Electro-Fenton Process Using a Stable $NiSe_2$ Cathode. *Nat. Catal.* **2022**, *5*, 716-725.

(25) Ross, R. D.; Sheng, H.; Parihar, A.; Huang, J.; Jin, S., Compositionally Tuned Trimetallic Thiospinel Catalysts for Enhanced Electrosynthesis of Hydrogen Peroxide and Built-In Hydroxyl Radical Generation. *ACS Catal.* **2021**, *11*, 12643-12650.

(26) Li, H.; Wen, P.; Itanze, D. S.; Hood, Z. D.; Adhikari, S.; Lu, C.; Ma, X.; Dun, C.; Jiang, L.; Carroll, D. L.; Qiu, Y.; Geyer, S. M., Scalable Neutral H_2O_2 Electrosynthesis

by Platinum Diphosphide Nanocrystals by Regulating Oxygen Reduction Reaction Pathways. *Nat. Commun.* **2020**, *11*, 3928.

(27) Yang, C.; Bai, S.; Yu, Z.; Feng, Y.; Huang, B.; Lu, Q.; Wu, T.; Sun, M.; Zhu, T.; Cheng, C.; Zhang, L.; Shao, Q.; Huang, X., A Newly-Explored Pd-Based Nanocrystal for the pH-Universal Electrosynthesis of H_2O_2. *Nano Energy* **2021**, *89*, 106480.

(28) Qiang, Z.; Chang, J.-H.; Huang, C.-P., Electrochemical Generation of Hydrogen Peroxide from Dissolved Oxygen in Acidic Solutions. *Water Res.* **2002**, *36*, 85-94.

(29) Brillas, E.; Sirés, I.; Oturan, M. A., Electro-Fenton Process and Related Electrochemical Technologies Based on Fenton's Reaction Chemistry. *Chem. Rev.* **2009**, *109*, 6570-6631.

(30) Zhao, X.; Wang, Y.; Da, Y.; Wang, X.; Wang, T.; Xu, M.; He, X.; Zhou, W.; Li, Y.; Coleman, J. N.; Li, Y., Selective Electrochemical Production of Hydrogen Peroxide at Zigzag Edges of Exfoliated Molybdenum Telluride Nanoflakes. *Natl. Sci. Rev.* **2020**, *7*, 1360-1366.

(31) Zhang, L.; Liang, J.; Yue, L.; Dong, K.; Xu, Z.; Li, T.; Liu, Q.; Luo, Y.; Liu, Y.; Gao, S.; Asiri, A. M.; Kong, Q.; Guo, X.; Sun, X., CoTe Nanoparticle-Embedded N-Doped Hollow Carbon Polyhedron: An Efficient Catalyst for H_2O_2 Electrosynthesis in Acidic Media. *J. Mater. Chem. A* **2021**, *9*, 21703-21707.

(32) Liang, J.; Wang, Y.; Liu, Q.; Luo, Y.; Li, T.; Zhao, H.; Lu, S.; Zhang, F.; Asiri, A. M.; Liu, F.; Ma, D.; Sun, X., Electrocatalytic Hydrogen Peroxide Production in Acidic Media Enabled by NiS_2 Nanosheets. *J. Mater. Chem. A* **2021**, *9*, 6117-6122.

(33) Yan, L.; Cheng, X.; Wang, Y.; Wang, Z.; Zheng, L.; Yan, Y.; Lu, Y.; Sun, S.; Qiu, W.; Chen, G., Exsolved Co_3O_4 with Tunable Oxygen Vacancies for Electrocatalytic H_2O_2 Production. *Mater. Today Energy* **2022**, *24*, 100931.

(34) Kulkarni, A.; Siahrostami, S.; Patel, A.; Nørskov, J. K., Understanding Catalytic Activity Trends in the Oxygen Reduction Reaction. *Chem. Rev.* **2018**, *118*, 2302-2312.

(35) Back, S.; Na, J.; Ulissi, Z. W., Efficient Discovery of Active, Selective, and Stable Catalysts for Electrochemical H_2O_2 Synthesis through Active Motif Screening. *ACS Catal.* **2021**, *11*, 2483-2491.

(36) Ford, D. C.; Nilekar, A. U.; Xu, Y.; Mavrikakis, M., Partial and Complete Reduction of O_2 by Hydrogen on Transition Metal Surfaces. *Surf. Sci.* **2010**, *604*, 1565-1575.

(37) Chen, Q.; Ma, C.; Yan, S.; Liang, J.; Dong, K.; Luo, Y.; Liu, Q.; Li, T.; Wang, Y.; Yue, L.; Zheng, B.; Liu, Y.; Gao, S.; Jiang, Z.; Li, W.; Sun, X., Greatly Facilitated Two-Electron Electroreduction of Oxygen into Hydrogen Peroxide over TiO_2 by Mn Doping. *ACS Appl. Mater. Interfaces* **2021**, *13*, 46659-46664.

(38) Dong, K.; Liang, J.; Wang, Y.; Ren, Y.; Xu, Z.; Zhou, H.; Li, L.; Liu, Q.; Luo, Y.; Li, T.; Asiri, A. M.; Li, Q.; Ma, D.; Sun, X., Plasma-Induced Defective TiO_{2-x} with Oxygen Vacancies: A High-Active and Robust Bifunctional Catalyst toward H_2O_2 Electrosynthesis. *Chem Catal.* **2021**, *1*, 1437-1448.

(39) Pourbaix Diagram. The Materials Project. https://legacy.materialsproject.org/#apps/pourbaixdiagram/ (accessed July 14, 2022).

(40) The Materials Project API. https://materialsproject.org/api (accessed July 14, 2022).

(41) Singh, A. K.; Zhou, L.; Shinde, A.; Suram, S. K.; Montoya, J. H.; Winston, D.; Gregoire, J. M.; Persson, K. A., Electrochemical Stability of Metastable Materials. *Chem. Mater.* **2017**, *29*, 10159-10167.

(42) Hansen, H. A.; Rossmeisl, J.; Nørskov, J. K., Surface Pourbaix Diagrams and Oxygen Reduction Activity of Pt, Ag and Ni(111) Surfaces Studied by DFT. *Phys. Chem. Chem. Phys.* **2008**, *10*, 3722-3730.

(43) Li, H.; Reuter, K., Ab Initio Thermodynamic Stability of Carbide Catalysts under Electrochemical Conditions. *ACS Catal.* **2022**, *12*, 10506-10513.

(44) Wang, Z.; Zheng, Y.-R.; Montoya, J.; Hochfilzer, D.; Cao, A.; Kibsgaard, J.; Chorkendorff, I.; Nørskov, J. K., Origins of the Instability of Nonprecious Hydrogen Evolution Reaction Catalysts at Open-Circuit Potential. *ACS Energy Lett.* **2021**, *6*, 2268-2274.

(45) Wang, Z.; Zheng, Y.-R.; Chorkendorff, I.; Nørskov, J. K., Acid-Stable Oxides for Oxygen Electrocatalysis. *ACS Energy Lett.* **2020**, *5*, 2905-2908.

(46) Zhao, W.-W.; Bothra, P.; Lu, Z.; Li, Y.; Mei, L.-P.; Liu, K.; Zhao, Z.; Chen, G.; Back, S.; Siahrostami, S.; Kulkarni, A.; Nørskov, J. K.; Bajdich, M.; Cui, Y., Improved Oxygen Reduction Reaction Activity of Nanostructured CoS_2 through Electrochemical Tuning. *ACS Appl. Energy Mater.* **2019**, *2*, 8605-8614.

(47) Zhou, R.; Zheng, Y.; Jaroniec, M.; Qiao, S.-Z., Determination of the Electron Transfer Number for the Oxygen Reduction Reaction: From Theory to Experiment. *ACS Catal.* **2016**, *6*, 4720-4728.

(48) Zhang, X.-L.; Su, X.; Zheng, Y.-R.; Hu, S.-J.; Shi, L.; Gao, F.-Y.; Yang, P.-P.; Niu, Z.-Z.; Wu, Z.-Z.; Qin, S.; Wu, R.; Duan, Y.; Gu, C.; Zheng, X.-S.; Zhu, J.-F.; Gao, M.-R., Strongly Coupled Cobalt Diselenide Monolayers for Selective Electrocatalytic Oxygen Reduction to H_2O_2 under Acidic Conditions. *Angew. Chem. Int. Ed.* **2021**, *60*, 26922-26931.

(49) Jung, E.; Shin, H.; Lee, B.-H.; Efremov, V.; Lee, S.; Lee, H. S.; Kim, J.; Hooch Antink, W.; Park, S.; Lee, K.-S.; Cho, S.-P.; Yoo, J. S.; Sung, Y.-E.; Hyeon, T., Atomic-Level Tuning of Co–N–C Catalyst for High-Performance Electrochemical H_2O_2 Production. *Nat. Mater.* **2020**, *19*, 436-442.

(50) Choi, C. H.; Kim, M.; Kwon, H. C.; Cho, S. J.; Yun, S.; Kim, H.-T.; Mayrhofer, K. J. J.; Kim, H.; Choi, M., Tuning Selectivity of Electrochemical Reactions by Atomically Dispersed Platinum Catalyst. *Nat. Commun.* **2016**, *7*, 10922.

(51) Tang, C.; Jiao, Y.; Shi, B.; Liu, J.-N.; Xie, Z.; Chen, X.; Zhang, Q.; Qiao, S.-Z., Coordination Tunes Selectivity: Two-Electron Oxygen Reduction on High-Loading Molybdenum Single-Atom Catalysts. *Angew. Chem. Int. Ed.* **2020**, *59*, 9171-9176.

(52) Tang, C.; Chen, L.; Li, H.; Li, L.; Jiao, Y.; Zheng, Y.; Xu, H.; Davey, K.; Qiao, S.-Z., Tailoring Acidic Oxygen Reduction Selectivity on Single-Atom Catalysts via Modification of First and Second Coordination Spheres. *J. Am. Chem. Soc.* **2021**, *143*, 7819-7827.

(53) Zhang, J.; Sasaki, K.; Sutter, E.; Adzic, R. R., Stabilization of Platinum Oxygen-Reduction Electrocatalysts Using Gold Clusters. *Science* **2007**, *315*, 220-222.

(54) Geiger, S.; Kasian, O.; Ledendecker, M.; Pizzutilo, E.; Mingers, A. M.; Fu, W. T.; Diaz-Morales, O.; Li, Z.; Oellers, T.; Fruchter, L.; Ludwig, A.; Mayrhofer, K. J. J.;

Koper, M. T. M.; Cherevko, S., The Stability Number as a Metric for Electrocatalyst Stability Benchmarking. *Nat. Catal.* **2018**, *1*, 508-515.

(55) Lopes, P. P.; Strmcnik, D.; Tripkovic, D.; Connell, J. G.; Stamenkovic, V.; Markovic, N. M., Relationships between Atomic Level Surface Structure and Stability/Activity of Platinum Surface Atoms in Aqueous Environments. *ACS Catal.* **2016**, *6*, 2536-2544.

(56) Chung, D. Y.; Lopes, P. P.; Farinazzo Bergamo Dias Martins, P.; He, H.; Kawaguchi, T.; Zapol, P.; You, H.; Tripkovic, D.; Strmcnik, D.; Zhu, Y.; Seifert, S.; Lee, S.; Stamenkovic, V. R.; Markovic, N. M., Dynamic Stability of Active Sites in Hydr(oxy)oxides for the Oxygen Evolution Reaction. *Nat. Energy* **2020**, *5*, 222-230.

(57) Lopes, P. P.; Li, D.; Lv, H.; Wang, C.; Tripkovic, D.; Zhu, Y.; Schimmenti, R.; Daimon, H.; Kang, Y.; Snyder, J.; Becknell, N.; More, K. L.; Strmcnik, D.; Markovic, N. M.; Mavrikakis, M.; Stamenkovic, V. R., Eliminating Dissolution of Platinum-Based Electrocatalysts at the Atomic Scale. *Nat. Mater.* **2020**, *19*, 1207-1214.

(58) Dam, V. A. T.; de Bruijn, F. A., The Stability of PEMFC Electrodes: Platinum Dissolution vs Potential and Temperature Investigated by Quartz Crystal Microbalance. *J. Electrochem. Soc.* **2007**, *154*, B494.

(59) Stewart, K. L.; Gewirth, A. A., Mechanism of Electrochemical Reduction of Hydrogen Peroxide on Copper in Acidic Sulfate Solutions. *Langmuir* **2007**, *23*, 9911-9918.

(60) Gill, T. M.; Zheng, X., Comparing Methods for Quantifying Electrochemically Accumulated H_2O_2. *Chem. Mater.* **2020**, *32*, 6285-6294.

(61) Jung, E.; Shin, H.; Hooch Antink, W.; Sung, Y.-E.; Hyeon, T., Recent Advances in Electrochemical Oxygen Reduction to H_2O_2: Catalyst and Cell Design. *ACS Energy Lett.* **2020**, *5*, 1881-1892.

(62) Zhang, X.; Xia, Y.; Xia, C.; Wang, H., Insights into Practical-Scale Electrochemical H_2O_2 Synthesis. *Trends Chem.* **2020**, *2*, 942-953.

(63) Tang, J.; Zhao, T.; Solanki, D.; Miao, X.; Zhou, W.; Hu, S., Selective Hydrogen Peroxide Conversion Tailored by Surface, Interface, and Device Engineering. *Joule* **2021**, *5*, 1432-1461.

(64) Wen, Y.; Zhang, T.; Wang, J.; Pan, Z.; Wang, T.; Yamashita, H.; Qian, X.; Zhao, Y., Electrochemical Reactors for Continuously Decentralized H_2O_2 Production. *Angew. Chem. Int. Ed.* **2022**, *61*, e202205972.

(65) Du, N.; Roy, C.; Peach, R.; Turnbull, M.; Thiele, S.; Bock, C., Anion-Exchange Membrane Water Electrolyzers. *Chem. Rev.* **2022**, *122*, 11830-11895.

(66) Lees, E. W.; Mowbray, B. A. W.; Parlane, F. G. L.; Berlinguette, C. P., Gas Diffusion Electrodes and Membranes for CO_2 Reduction Electrolysers. *Nat. Rev. Mater.* **2022**, *7*, 55-64.

(67) Zhang, X.; Zhao, X.; Zhu, P.; Adler, Z.; Wu, Z.-Y.; Liu, Y.; Wang, H., Electrochemical Oxygen Reduction to Hydrogen Peroxide at Practical Rates in Strong Acidic Media. *Nat. Commun.* **2022**, *13*, 2880.

(68) Ehelebe, K.; Schmitt, N.; Sievers, G.; Jensen, A. W.; Hrnjić, A.; Collantes Jiménez, P.; Kaiser, P.; Geuß, M.; Ku, Y.-P.; Jovanovič, P.; Mayrhofer, K. J. J.; Etzold, B.; Hodnik, N.; Escudero-Escribano, M.; Arenz, M.; Cherevko, S., Benchmarking Fuel Cell

Electrocatalysts Using Gas Diffusion Electrodes: Inter-lab Comparison and Best Practices. *ACS Energy Lett.* **2022**, *7*, 816-826.

(69) Lee, S. H.; Kim, J.; Chung, D. Y.; Yoo, J. M.; Lee, H. S.; Kim, M. J.; Mun, B. S.; Kwon, S. G.; Sung, Y.-E.; Hyeon, T., Design Principle of Fe–N–C Electrocatalysts: How to Optimize Multimodal Porous Structures? *J. Am. Chem. Soc.* **2019**, *141*, 2035-2045.

(70) Mariano, R. G.; Wahab, O. J.; Rabinowitz, J. A.; Oppenheim, J.; Chen, T.; Unwin, P. R.; Dincă, M., Thousand-fold increase in O_2 electroreduction rates with conductive MOFs. *ACS Cent. Sci.* **2022**, *8*, 975-982.

(71) Osmieri, L.; Wang, G.; Cetinbas, F. C.; Khandavalli, S.; Park, J.; Medina, S.; Mauger, S. A.; Ulsh, M.; Pylypenko, S.; Myers, D. J.; Neyerlin, K. C., Utilizing ink composition to tune bulk-electrode gas transport, performance, and operational robustness for a Fe–N–C catalyst in polymer electrolyte fuel cell. *Nano Energy* **2020**, *75*, 104943.

(72) Berlinger, S. A.; McCloskey, B. D.; Weber, A. Z., Probing Ionomer Interactions with Electrocatalyst Particles in Solution. *ACS Energy Lett.* **2021**, *6*, 2275-2282.

(73) Zhang, Q.; Zhou, M.; Ren, G.; Li, Y.; Li, Y.; Du, X., Highly Efficient Electrosynthesis of Hydrogen Peroxide on a Superhydrophobic Three-Phase Interface by Natural Air Diffusion. *Nat. Commun.* **2020**, *11*, 1731.

(74) Li, H.; Quispe-Cardenas, E.; Yang, S.; Yin, L.; Yang, Y., Electrosynthesis of >20 g/L H_2O_2 from Air. *ACS ES&T Eng.* **2022**, *2*, 242-250.

(75) Xia, Y.; Zhao, X.; Xia, C.; Wu, Z.-Y.; Zhu, P.; Kim, J. Y.; Bai, X.; Gao, G.; Hu, Y.; Zhong, J.; Liu, Y.; Wang, H., Highly Active and Selective Oxygen Reduction to H_2O_2 on Boron-Doped Carbon for High Production Rates. *Nat. Commun.* **2021**, *12*, 4225.

(76) Alia, S. M.; Reeves, K. S.; Baxter, J. S.; Cullen, D. A., The Impact of Ink and Spray Variables on Catalyst Layer Properties, Electrolyzer Performance, and Electrolyzer Durability. *J. Electrochem. Soc.* **2020**, *167*, 144512.

(77) Ridruejo, C.; Alcaide, F.; Álvarez, G.; Brillas, E.; Sirés, I., On-Site H_2O_2 Electrogeneration at a CoS_2-Based Air-Diffusion Cathode for the Electrochemical Degradation of Organic Pollutants. *J. Electroanal. Chem.* **2018**, *808*, 364-371.

(78) Alcaide, F.; Álvarez, G.; Guelfi, D. R. V.; Brillas, E.; Sirés, I., A Stable CoSP/MWCNTs Air-Diffusion Cathode for the Photoelectro-Fenton Degradation of Organic Pollutants at Pre-Pilot Scale. *Chem. Eng. J.* **2020**, *379*, 122417.

(79) Sun, J.; Dai, X.; Wang, Q.; van Loosdrecht, M. C. M.; Ni, B.-J., Microplastics in Wastewater Treatment Plants: Detection, Occurrence and Removal. *Water Res.* **2019**, *152*, 21-37.

(80) Tagg, A. S.; Harrison, J. P.; Ju-Nam, Y.; Sapp, M.; Bradley, E. L.; Sinclair, C. J.; Ojeda, J. J., Fenton's Reagent for the Rapid and Efficient Isolation of Microplastics from Wastewater. *Chem. Commun.* **2017**, *53*, 372-375.

(81) Wang, J.-c.; Wang, H., Fenton Treatment for Flotation Separation of Polyvinyl Chloride from Plastic Mixtures. *Sep. Purif. Technol.* **2017**, *187*, 415-425.

(82) Lucas, F. W. S.; Grim, R. G.; Tacey, S. A.; Downes, C. A.; Hasse, J.; Roman, A. M.; Farberow, C. A.; Schaidle, J. A.; Holewinski, A., Electrochemical Routes for the Valorization of Biomass-Derived Feedstocks: From Chemistry to Application. *ACS Energy Lett.* **2021**, *6*, 1205-1270.

(83) Teong, S. P.; Li, X.; Zhang, Y., Hydrogen Peroxide as an Oxidant in Biomass-to-Chemical Processes of Industrial Interest. *Green Chem.* **2019**, *21*, 5753-5780.

(84) Liu, W.-J.; Dang, L.; Xu, Z.; Yu, H.-Q.; Jin, S.; Huber, G. W., Electrochemical Oxidation of 5-Hydroxymethylfurfural with NiFe Layered Double Hydroxide (LDH) Nanosheet Catalysts. *ACS Catal.* **2018**, *8*, 5533-5541.

(85) Liu, W.-J.; Xu, Z.; Zhao, D.; Pan, X.-Q.; Li, H.-C.; Hu, X.; Fan, Z.-Y.; Wang, W.-K.; Zhao, G.-H.; Jin, S.; Huber, G. W.; Yu, H.-Q., Efficient Electrochemical Production of Glucaric Acid and H_2 via Glucose Electrolysis. *Nat. Commun.* **2020**, *11*, 265.

(86) Han, X.; Sheng, H.; Yu, C.; Walker, T. W.; Huber, G. W.; Qiu, J.; Jin, S., Electrocatalytic Oxidation of Glycerol to Formic Acid by $CuCo_2O_4$ Spinel Oxide Nanostructure Catalysts. *ACS Catal.* **2020**, *10*, 6741-6752.

(87) Perryman, J. T.; Velázquez, J. M., Design Principles for Multinary Metal Chalcogenides: Toward Programmable Reactivity in Energy Conversion. *Chem. Mater.* **2021**, *33*, 7133-7147.

(88) Xia, F.; Li, B.; Liu, Y.; Liu, Y.; Gao, S.; Lu, K.; Kaelin, J.; Wang, R.; Marks, T. J.; Cheng, Y., Carbon Free and Noble Metal Free $Ni_2Mo_6S_8$ Electrocatalyst for Selective Electrosynthesis of H_2O_2. *Adv. Funct. Mater.* **2021**, *31*, 2104716.

(89) Jin, S., Are Metal Chalcogenides, Nitrides, and Phosphides Oxygen Evolution Catalysts or Bifunctional Catalysts? *ACS Energy Lett.* **2017**, *2*, 1937-1938.

(90) Kelly, S. R.; Kirk, C.; Chan, K.; Nørskov, J. K., Electric Field Effects in Oxygen Reduction Kinetics: Rationalizing pH Dependence at the Pt(111), Au(111), and Au(100) Electrodes. *J. Phys. Chem. C* **2020**, *124*, 14581-14591.

(91) Kim, H. W.; Bukas, V. J.; Park, H.; Park, S.; Diederichsen, K. M.; Lim, J.; Cho, Y. H.; Kim, J.; Kim, W.; Han, T. H.; Voss, J.; Luntz, A. C.; McCloskey, B. D., Mechanisms of Two-Electron and Four-Electron Electrochemical Oxygen Reduction Reactions at Nitrogen-Doped Reduced Graphene Oxide. *ACS Catal.* **2020**, *10*, 852-863.

(92) Rao, K. K.; Lai, Y.; Zhou, L.; Haber, J. A.; Bajdich, M.; Gregoire, J. M., Overcoming Hurdles in Oxygen Evolution Catalyst Discovery via Codesign. *Chem. Mater.* **2022**, *34*, 899-910.

(93) Nayak, S.; McPherson, I. J.; Vincent, K. A., Adsorbed Intermediates in Oxygen Reduction on Platinum Nanoparticles Observed by In Situ IR Spectroscopy. *Angew. Chem. Int. Ed.* **2018**, *57*, 12855-12858.

(94) Casalongue, H. S.; Kaya, S.; Viswanathan, V.; Miller, D. J.; Friebel, D.; Hansen, H. A.; Nørskov, J. K.; Nilsson, A.; Ogasawara, H., Direct Observation of the Oxygenated Species during Oxygen Reduction on a Platinum Fuel Cell Cathode. *Nat. Commun.* **2013**, *4*, 2817.